J. Fluid Mech. (2001), *vol.* 429, *pp.* 117–153. Printed in the United Kingdom

Swirling flow of viscoelastic fluids. Part 2. Elastic effects

By JASON R. STOKES[1], LACHLAN J. W. GRAHAM[2], NICK J. LAWSON[1] AND DAVID V. BOGER[1]

[1]Department of Chemical Engineering, The University of Melbourne, Parkville 3052, Australia

[2]Advanced Fluid Dynamics Laboratory, CSIRO Building Construction and Engineering, Graham Road, Highett 3190, Australia

(Received 29 December 1998 and in revised form 11 October 1999)

A torsionally driven cavity has been used to examine the influence of elasticity on the swirling flow of constant-viscosity elastic liquids (Boger fluids). A wealth of phenomena is observed as the degree of inertia, elasticity and viscous forces are varied by using a range of low- to high-viscosity flexible polyacrylamide Boger fluids and a semi-rigid xanthan gum Boger fluid. As the inertia is decreased and elasticity increased by using polyacrylamide Boger fluids, the circulation rates for a 'Newtonian-like' secondary flow decreases until flow reversal occurs owing to the increasing magnitude of the primary normal stress difference. For each polyacrylamide fluid, the flow becomes highly unstable at a critical combination of Reynolds number and Weissenberg number resulting in a new time-dependent elastic instability. Each fluid is characterized by a dimensionless elasticity number and a correlation with Reynolds number is found for the occurrence of the instability. In the elasticity dominated flow of the polyacrylamide Boger fluids, the instability disrupts the flow dramatically and causes an increase in the peak axial velocity along the central axis by as much as 400%. In this case, the core vortex spirals with the primary motion of fluid and is observed in some cases at Reynolds numbers much less than unity. Elastic 'reverse' flow is observed for the xanthan gum Boger fluid at high Weissenberg number. As the Weissenberg number decreases, and Reynolds number increases, counter-rotating vortices flowing in the inertial direction form on the rotating lid. The peak axial velocity decreases for the xanthan gum Boger fluid with decreasing Weissenberg number. In addition, several constitutive models are used to describe accurately the rheological properties of the fluids used in this work in shear and extensional flow. This experimental investigation of a complex three-dimensional flow using well-characterized fluids provides the information necessary for the validation of non-Newtonian constitutive models through numerical analysis of the torsionally driven cavity flow.

1. Introduction

The confined swirling flow of elastic fluids in an enclosed cylindrical vessel with a rotating bottom lid provides a complex flow field in a simple geometry, which is suitable for comparison with numerical models. Also, swirling flow of non-Newtonian fluids is common throughout process engineering applications and, hence, an understanding of the behaviour of elastic fluids in a well-defined swirling flow situation is highly beneficial. The ability to predict the behaviour of the flow of elastic liquids

will enable the validation of non-Newtonian constitutive models and act as precursor to solving more difficult geometries involving swirl. The previous work on confined swirling flow was reviewed in Part 1 (Stokes *et al.* 2001) and will not be repeated here.

The previous experimental investigations into confined swirling flow of non-Newtonian fluids have been conducted using shear-thinning fluids with varying degrees of elasticity (Hill 1972; Böhme, Rubart & Stenger 1992; Day *et al.* 1996; Wünshch & Böhme 1996; Escudier & Cullen 1997). The success of numerical investigations to predict the flow behaviour of non-Newtonian fluids in confined swirling flow has been limited, such that few of the experimental observations have been predicted to occur (Kramer & Johnson 1972; Nirschl & Stewart 1984; Chiao & Chang 1990; Böhme *et al.* 1992; Escudier & Cullen 1996; Wünshch & Böhme 1996). This was, in part, due to the difficulty of discriminating between effects on the flow kinematics owing to shear thinning and those associated with elasticity in the experimental results. Therefore, there is a need for experimental data using well-characterized constant-viscosity elastic fluids, i.e. Boger fluids (Boger 1977/78), to remove any effects due to shear thinning. Low-viscosity Boger fluids are used in Part 1 to examine the influence of up to 75 p.p.m. of polymer (polyacrylamide or xanthan gum) in an inertia-dominated flow where axisymmetric vortex breakdown is present for Newtonian fluids. Part 2 examines experimentally the swirling flow of medium- to high-viscosity elastic fluids for conditions ranging from where inertia is dominating to where elasticity is dominant across the flow field.

2. Experimental

A detailed description of the experimental set-up and apparatus may be found in Part 1.

2.1. *Experimental set-up and apparatus*

The experimental apparatus consisted of an acrylic cylinder, located in a rectangular acrylic water bath, with a rotating stainless steel base and stationary top lid. Laser flow visualization was used to observe streamlines by injecting fluorescent dye or particles into the flow cell with a laser light sheet. Particle image velocimetry (PIV) was also used to map the velocity flow field in a given vertical plane. The technique used multiple-exposure photography with flourescent particles as tracers, and digital autocorrelation techniques for data processing.

The characteristic dimensionless numbers defined previously in Part 1 are the Reynolds number ($Re = \rho 2\pi\Omega R^2/\eta$), Weissenberg number ($We = \lambda_M 2\pi\Omega$), elasticity number ($El = We/Re = \lambda_M \eta/\rho R^2$), and aspect ratio ($H/R$). The characteristic time of the fluid is taken as the Maxwell relaxation time ($\lambda_M = \Psi_1/2\eta$) where Ψ_1 is the primary normal stress coefficient.

2.2. *Test fluids*

The polymers used in the test fluids were dilute concentrations of Separan AP30 and MG500 polyacrylamides (PAA) and a semi-dilute concentration of Koltrol xanthan gum (XG). Their corresponding molecular weights were measured as 3.1 million, 3.6 million and 6.3 million, respectively (Stokes 1998; Stokes *et al.* 2001). The viscous Newtonian solvents used were either glycerol or 43°Be wheat syrup (supplied by Weston Bioproducts) mixed with water. Sodium chloride was also added to some solutions. The polymer concentration, solvent viscosity, and solvent quality were all

	Polymer		Viscous solvent		Water	Salt (NaCl)
Label	Type	Wt%	Type	Wt%	Wt%	Wt%
A	PAA AP30	0.015	Glycerol	82	15.24	2.73
B	PAA AP30	0.015	Glycerol	90	8.31	1.66
C	PAA AP30	0.015	Wheat syrup	85	14.97	—
D	PAA AP30	0.025	Wheat syrup	88	11.96	—
E	PAA AP30	0.0396	Wheat syrup	93	6.94	—
XG	XG Keltrol	0.02	Wheat syrup	92	7.96	—

TABLE 1. Test fluid compositions.

manipulated in order to obtain a range of fluids with a constant relaxation time at low shear rates and an elasticity number spanning several orders of magnitude. The fluids and their compositions are given in table 1 and were made using a similar method to that described in Part 1. Sodium azide (NaN_3) was used at a concentration of 0.02 wt% for all solutions, to act as a biocide.

2.3. *Rheology*

The rheological measurements consisted of characterizing the steady state shear and dynamic properties using rheometers with a cone-and-plate configuration, and extensional properties using an opposed jet apparatus and a filament stretching device. The cone and plate instruments included a Weissenberg R19 rheogiometer with a 7 cm cone and 2.4° cone angle and a Weissenberg R20 rheogiometer with 5 cm cone and 2° cone angle which were operated in temperature-controlled rooms. The Weissenberg rheogiometers are constant-shear-rate devices and were used to measure the viscosity, primary normal stress difference and dynamic properties (loss and storage moduli). A Carri-Med CSL 100 constant stress cone and plate rheometer was used with various cone and plate sizes, and a peltier temperature control, to determine the viscosity and the dynamic properties of the test fluids. Evaporation of the sample during rheological measurements was minimized by the application of a thin layer of an inert silicone oil, of comparable viscosity to the test fluid, to the outer edge of the sample. Apparent extensional viscosities were measured using a Rheometrics RFX opposed jet apparatus. The uniaxial extensional viscosity was measured in a filament stretching device for several of the test fluids by Duc At Nguyen at Monash University. All the following measurements are presented for $20 \pm 0.25\,^{\circ}\mathrm{C}$.

The rheological properties measured for all the Boger fluids are shown in figures 1 to 5. These properties are summarized in tables 2 and 3 with the aid of the power-law model to describe the degree of shear thinning for each fluid with a characteristic relaxation time evaluated using the Maxwell model (Bird, Armstrong & Hassanger 1987*a*). The steady shear properties for the five polyacrylamide Boger fluids are presented in figure 1. All the polyacrylamide solutions have a constant viscosity and the slope for the shear stress (τ)–shear rate ($\dot{\gamma}$) curves are all close to unity. At low shear rates, the primary normal stress difference (N_1) curves all show quadratic dependence on the shear rate such that the primary normal stress coefficient ($\Psi_1 = N_1/\dot{\gamma}^2$) approaches a plateau, as shown in figure 1(*b*). Hence, a constant Maxwell relaxation time for each polyacrylamide Boger fluid can be established at low shear rates which is subsequently used as the characteristic time of the fluids. The properties given in table 3 were used for defining the dimensionless numbers governing the flow of elastic liquids in the torsionally driven cavity. Confined swirling flow experiments were also

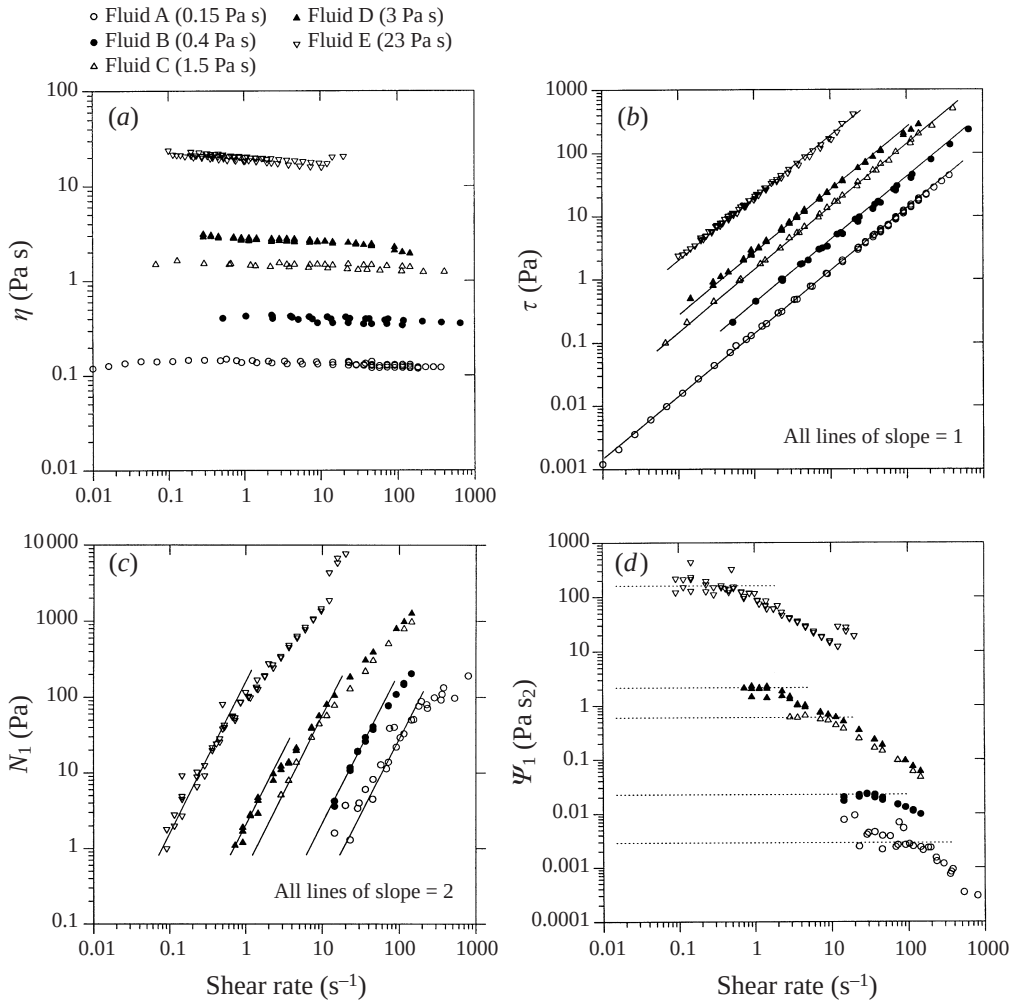

FIGURE 1. Steady shear properties for polyacrylamide Boger fluids indicating (*a*) viscosity, and (*b*) primary normal stress coefficient.

performed using a slightly shear-thinning polyacrylamide solution, labelled fluid Fst. The rheology for fluid Fst is detailed in Stokes (1998) and has a zero-shear rate viscosity of $\eta_0 = 1.1$ Pa s.

The dynamic properties for the polyacrylamide Boger fluids are shown in figure 2 as twice the storage modulus ($2G'$). The $2G'$ for the Newtonian solvents are all equal, to within 10%, and are presented in figure 2 as a single line (Stokes 1998). Limitations of the rheometers, however result in unreliable measurements for fluid A where the storage modulus is similar to that of the solvents. $2G'$ is used as the ordinate because simple fluid theory stipulates that (Bird *et al.* 1987*a*),

$$\lim_{\dot{\gamma}\to 0} N_1 \to \lim_{\omega\to 0} 2G'.$$

The extensional properties measured using the opposed jet apparatus for each polyacrylamide Boger fluid are shown in figure 3 as an apparent Trouton ratio ($Tr = \eta_e/\eta$). As mentioned in Part 1, the opposed jet rheometer only approximates an

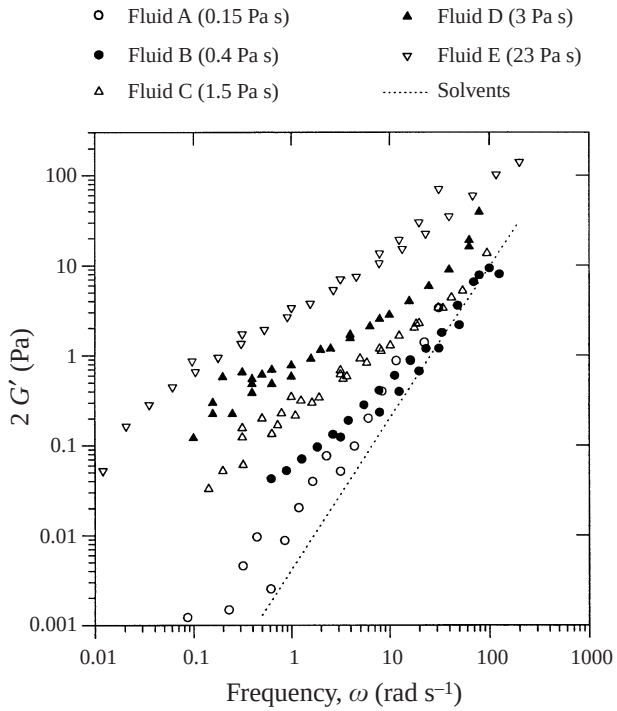

FIGURE 2. Dynamic property for polyacrylamide Boger fluids displayed as twice the storage modulus.

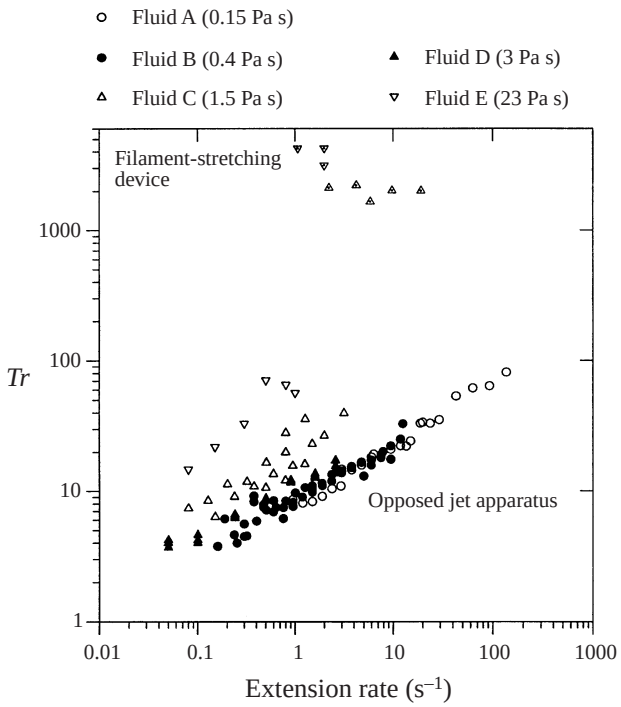

FIGURE 3. Extensional properties of the polyacrylamide Boger fluids as indicated by the Trouton ratio using the opposed jet rheometer and the filament stretching device (dotted symbols).

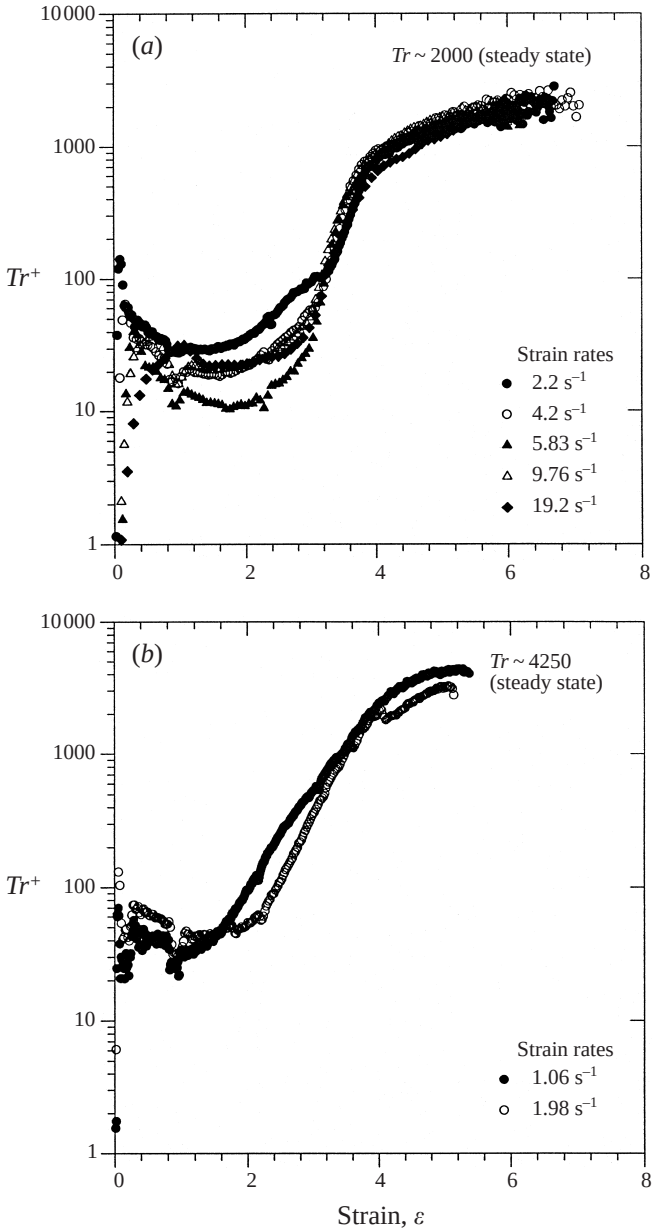

FIGURE 4. Uniaxial extensional stress growth indicated by the transient Trouton ratio as a function of strain for (*a*) polyacrylamide Boger fluid C and (*b*) polyacrylamide Boger fluid E, measured using the filament stretching device.

extensional flow field, so the results must be treated with some caution. Measurements from the opposed jet show that the polyacrylamide Boger fluids are strain-rate thickening with the maximum Trouton ratio measurable being only $Tr \approx 100$. Also shown in figure 3 is the Trouton ratio at steady state for polyacrylamide Boger fluids C and E measured using the filament-stretching device and indicated by dotted symbols. The steady-state extensional viscosity is obtained at high strains from figure 4 which

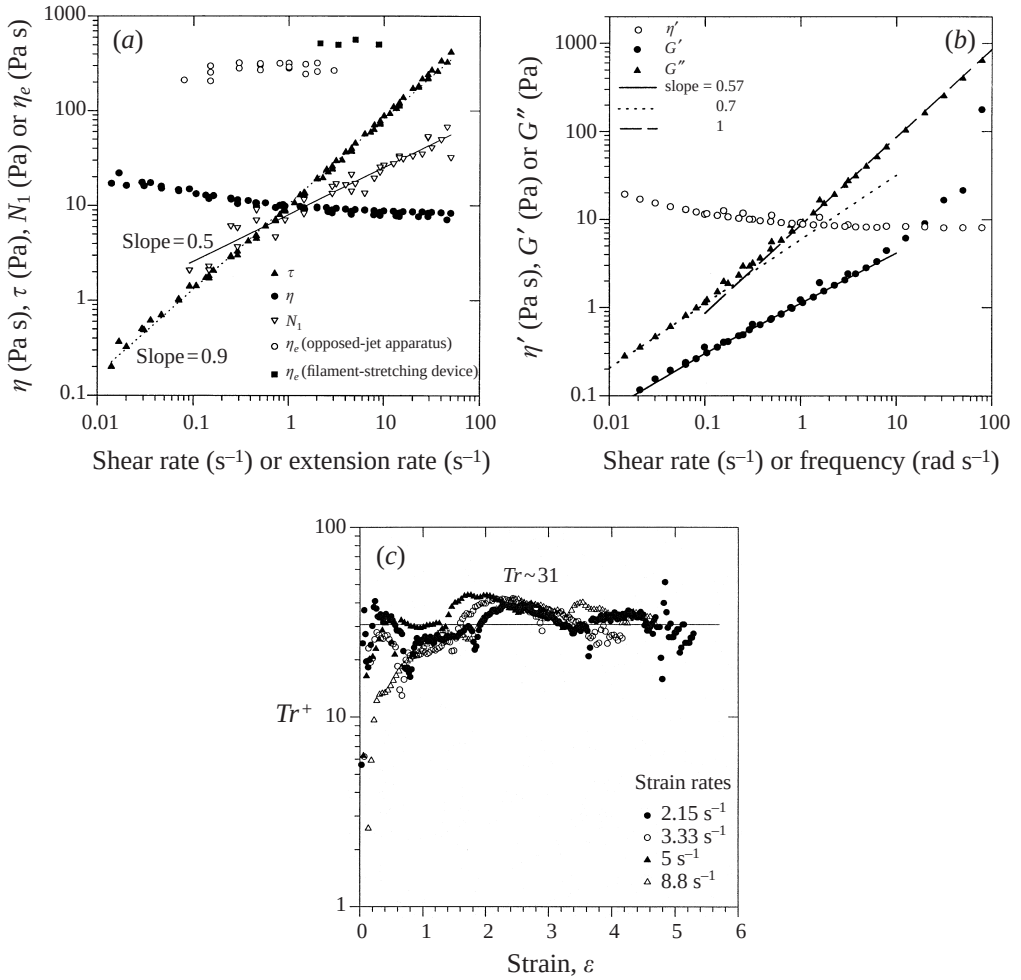

FIGURE 5. Rheological properties of the xanthan gum Boger fluid including (*a*) steady shear and extensional measurements, (*b*) small-amplitude oscillatory measurements, and (*c*) uniaxial extensional growth shown as a transient Trouton ratio.

Fluid	η_0 (Pa s)	η_S (Pa s)	K (Pa s^n)	n	$\Psi_{1,0}$ (Pa s^2)
A	0.15	0.12	0.135	0.981	0.0029
B	0.43	0.33	0.420	0.973	0.0224
C	1.5	1.13	1.442	0.977	0.6
D	3	1.2	2.82	0.947	2.16
E	23	10.4	19.7	0.949	160
XG	17	7.4	10.5	0.90	$7.9\dot{\gamma}^{-0.5}$

TABLE 2. Zero shear rate viscosity, solvent viscosity, power law parameters and zero shear rate primary normal stress coefficient for test fluids. Power law parameters are defined such that $\eta = K\dot{\gamma}^{n-1}$.

Fluid	η (Pa s)	ρ (Kg m^{-3})	λ_M (s)	El
A	0.146	1232	0.01	0.24×10^{-3}
B	0.40	1247	0.028	1.8×10^{-3}
C	1.5	1348	0.2	45×10^{-3}
D	3	1380	0.36	0.16
E	23	1380	3.5	12
XG	17	1380	$3.95\dot{\gamma}^{-1.5}$	$0.58\dot{\gamma}^{-1.5}$

TABLE 3. Material properties used in defining the governing dimensionless numbers in the torsionally driven cavity for each test fluid. El is evaluated with $R = 0.07$ m.

shows the transient Trouton ratio (Tr^+) as a function of strain ($\varepsilon = \dot{\varepsilon}t$) for fluids C and E. The filament-stretching device generates a true uniaxial flow field, and figure 4 shows the growth of the Trouton ratio with strain to constant steady-state values of $Tr \approx 2000$ and $Tr \approx 4250$ for fluids C and E, respectively. Within a narrow range of strain rates, $1\,\mathrm{s}^{-1} < \dot{\varepsilon} < 20\,\mathrm{s}^{-1}$, these steady-state values are essentially independent of strain rate. The Trouton ratio at low strains for fluids C and E is above what has been typically observed for other Boger fluids where the Trouton ratio is observed to gradually rise with strain rate from a value of $Tr \approx 3$ (Tirtaatmadja & Sridhar 1993). This anomaly is a result of the low viscosity of the fluids compared with those previously used in the filament-stretching device, and is probably the result of surface tension and end effects which are significant at the onset of the stretching experiment. Also, at low strains, the aspect ratio of the sample is less than one, which can also cause slightly higher than expected measurements. Another possible source of error includes evaporation of the sample and crystallization of the wheat syrup, causing the formation of a 'skin' on the surface. However, for high strains and when the extensional viscosity is large, all these effects become negligible, so the steady value reached at high strains is considered a reliable measurement of the extensional viscosity. The opposed-jet device measured lower Trouton ratios owing to the low strain in the flow which is of the order of one ($\varepsilon = O[1]$), so that the molecules had not reached their fully extended state.

The rheological properties for the xanthan gum Boger fluid are presented in figure 5. The viscosity is slightly shear thinning with a power-law exponent of 0.9 and a zero shear viscosity about a factor of two above the solvent viscosity. The slope of the normal stress curve is very different from that for polyacrylamide solutions. The primary normal stress difference depends on $\dot{\gamma}^{1/2}$, which is similar to that expected for dilute solutions of rigid rod-like molecules where N_1 is predicted to vary with $\dot{\gamma}^{2/3}$ (Bird *et al.* 1987*a*). The extensional viscosity is measured to be constant with strain rate and of similar magnitude using both the opposed-jet rheometer and filament-stretching device. The constant values result as the rigid macromolecules fully align along the flow field for all strain rates.

The dynamic properties for xanthan gum are presented in figure 5(*b*) in terms of the dynamic viscosity (η'), the storage modulus (G') and loss modulus (G''). The dynamic viscosity is shown to be relatively constant and the storage modulus varies with $\omega^{0.57}$ in a similar fashion to the dependence of N_1 on shear rate. The extensional stress growth is shown in figure 5(*c*) where the transient Trouton ratio fluctuates about a constant value with strain for all extension rates examined as the rigid macromolecules 'instantaneously' align with the extensional flow field on start up.

Material properties	Fluid A	Fluid B	Fluid C	Fluid D	Fluid E
η_s	0.12	0.33	1.13	1.2	10.4
η_ρ	0.026	0.07	0.37	1.8	12.6
λ_p	0.06	0.16	0.81	0.6	6.39
FENE-P					
B	250	860	800 4300*	60	350 3700*
Giesekus					
α	0.014	0.0006	5.97×10^{-4} 0.00025*	0.01	0.0025 0.00026*
KBKZ					
α	—	—	3000	—	4000
β	—	—	0.021	—	0.033

TABLE 4. Material properties for the polyacrylamide Boger fluids using the Oldroyd-B, FENE-P, Giesekus and KBKZ constitutive models for a single relaxation mode. * indicates that the parameter was determined from the steady-state extensional viscosity. η_i And λ_i have the units of (Pa s) and (s), respectively.

2.4. *Constitutive model parameters*

To be able to predict the behaviour of viscoelastic fluids in the torsionally driven cavity, the rheology of the fluids used must be described by non-Newtonian constitutive equations. The material properties for the polyacrylamide Boger fluids were predicted using the following constitutive models: Oldroyd-B (Oldroyd 1950), FENE-P (Peterlin 1966; Warner 1972; Bird, Dotson & Johnson 1980), Giesekus (Giesekus 1982, 1983; Bird & Weist 1985) and KBKZ (Kaye 1962; Bernstien, Kearsley & Zapas 1963; Papanastasiou, Scriven & Macosko 1983). Details on these models may be found in Stokes (1998) and throughout the literature (Bird *et al.* 1987*a*, *b*; Byars, Binnington & Boger 1997; Tirtaatmadja 1993; Tirtaatmadja & Sridhar 1995). The predictions of the rheological measurements using these models are beyond the scope of this publication. Stokes (1998) may be referred to for details on the model parameters for both single and multiple relaxation modes, and also for comparison with rheological measurements. Table 4 is included to show the model parameters for a single relaxation mode for the aforementioned models. These parameters were chosen to best fit the rheological data available in both shear and extension of the polyacrylamide Boger fluids. Therefore, the fluids used in this study have been described by several constitutive models which can then be used for predicting the flow behaviour of these fluids in the torsionally driven cavity.

The validity of the single mode rigid dumbbell model of Bird *et al.* (1987*b*) is investigated using the xanthan gum Boger fluid properties. The rigid dumbbell model is found to describe the dynamic properties of the fluid poorly, but a similar dependency on shear rate for the primary normal stress difference measurements is predicted (see Stokes 1998). The model also predicts a constant extensional viscosity equal to 430 Pa s which is within 20% of the measured value. The rigid dumbbell relaxation time ($\lambda_D = 102$ s) is calculated in the same manner as in Part 1. Therefore, in an extension dominated flow field, it is expected that this model may prove to be a suitable choice for describing rigid macromolecules. Further investigations are required, however, to choose the most appropriate model to describe the rigid xanthan gum Boger fluids in the torsionally driven cavity.

3. Results and discussion

Presentation and discussion of the experimental results are split into three sections. The first section examines the secondary flow behaviour using flexible polyacrylamide Boger fluids A and B which have low elasticity numbers of 0.0002 and 0.002, respectively, such that the flow is dominated by inertial forces. The second section examines the secondary flow field using polyacrylamide Boger fluids C, D and E which have medium to high elasticity numbers of 0.05, 0.16 and 12, respectively, such that elastic and viscous forces become increasingly more dominant. The third section examines the flow field for one highly viscous semi-rigid xanthan gum Boger fluid. The relaxation time for the xanthan gum fluid decreases with increasing shear rate such that the elasticity number varies from $El \approx 1$ to as high as $El \approx 130$ for the range of flow fields examined.

Terminology which is used to describe the secondary flow kinematics are 'Newtonian-like' or inertial flow vortex and 'reverse' or 'elastic' flow vortex as shown in figure 1 of Part 1. 'Newtonian-like' flow is when the fluid moves radially outwards along the rotating lid as dictated by centrifugal forces, up the sidewalls and down the central axis. Any vortex rotating in the same direction as the 'Newtonian-like' flow is termed an inertial vortex. The secondary flow where the fluid moves radially inwards is termed 'reverse' or 'elastic' flow because the vortex is rotating in the opposite direction to that for a Newtonian fluid.

3.1. *Elastic effects in an inertia dominated flow of flexible polymer Boger fluids*

The confined swirling flow of two Boger fluids, polyacrylamide fluids A and B, which have very low elasticity numbers of 0.0002 and 0.002, respectively, is dominated by inertial forces. Contrary to the low-viscosity Boger fluids used in Part 1, however, polyacrylamide fluids A and B are viscous and elastic enough such that steady shear elastic properties (i.e. N_1) are measurable. As will be described in the following, 'Newtonian-like' flow is observed for both fluids A and B but at a critical combination of Reynolds number and Weissenberg number (or elasticity number), the flow field is dramatically disrupted owing to the influence of elasticity such that the flow becomes unsteady.

Steady 'Newtonian-like' flow is observed at aspect ratios of $1 \leqslant H/R \leqslant 2$ for polyacrylamide fluid A at Reynolds numbers of $Re < 300$ ($We < 0.07$). The secondary flow regime for polyacrylamide fluid A becomes asymmetric for $Re > 300$ ($We > 0.07$) with one half of the circulating 'Newtonian-like' vortex smaller than the other half. At $Re \approx 380$ ($We \approx 0.09$), an instability with a non-discernible period occurs near the middle of the rotating disk. The instability takes one to two minutes to form after starting the rotation of the disk from rest and an interpretation of the kinematics is given in figure 6. The instability occurs over a number of seconds and follows a sequence in time where the flow is initially 'Newtonian-like' (figure 6*a*). A stagnant zone then forms abruptly in the region near the centre of the rotating disk causing waviness in the secondary flow regime and spiralling of the vortex core (figure 6*b*). Part of the fluid then travels upwards from the centre of the disk giving rise to a small recirculation zone (figure 6*c*). The sequence then reverses such that the flow becomes stagnant near the centre of the disk and 'Newtonian-like' secondary flow reoccurs. The flow field becomes highly irregular as the Reynolds number is increased. The instability is difficult to visualize because the fluorescent dye used in flow-visualization experiments disperses quickly owing to the low viscosity of the fluid and the unsteady flow behaviour. It is therefore difficult to examine the full characteristics of the instability, and further work is needed to characterize this feature in detail.

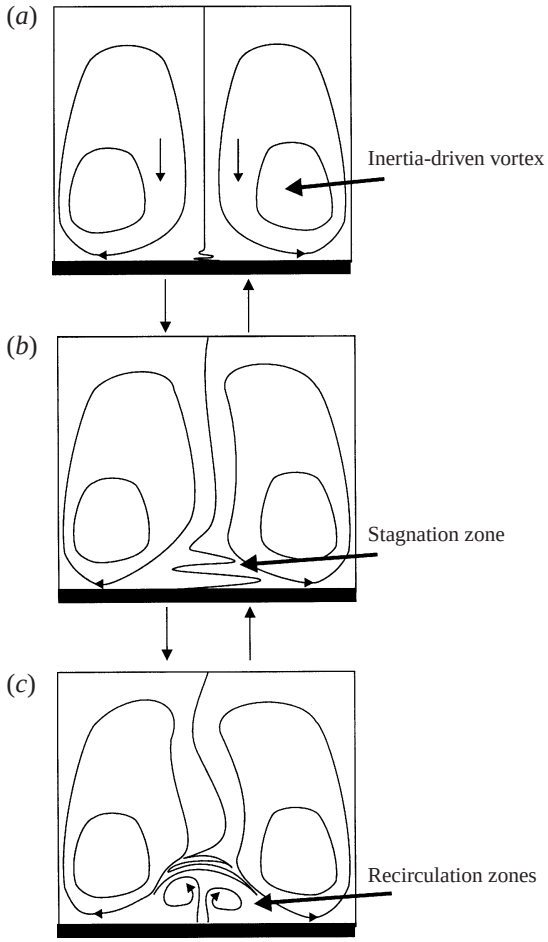

FIGURE 6. Representation of the unstable secondary flow field for polyacrylamide fluid A at $Re > 378$, $We > 0.089$ and $H/R = 2$ showing the cyclic transformation with time including (*a*) 'Newtonian-like' flow, (*b*) stagnation region near $r \approx 0$, and (*c*) region of 'reverse' flow.

PIV is used to obtain instantaneous radial and axial velocity profiles at Reynolds numbers before and after the occurrence of the unsteady flow field for fluid A. Figures 7 and 8 show the differences in the flow field in a steady state at $Re = 216$ ($We = 0.05$) and an unsteady state at $Re = 378$ ($We = 0.089$), respectively, using sectional streamline patterns and a contour plot of the azimuthal component of vorticity. Figure 7 illustrates the highly symmetrical and 'Newtonian-like' nature of the steady flow field, whereas figure 8 illustrates an asymmetrical vortex. The azimuthal vorticity consists of two cores of vorticity with opposite sign for the steady flow case in figure 7(*b*). However, when the flow is unsteady, as in figure 8(*b*), there is an additional core of vorticity on the left-hand side of opposite sign to the main vortex. This negative azimuthal vorticity is created as a result of the asymmetry in the flow and is essentially an extension of the right-hand side vortex.

The axial velocity along the centreline ($-5\,\text{mm} < r < 5\,\text{mm}$) is shown in figure 9 for polyacrylamide fluid A and compared to the velocity distributions for Newtonian fluids at similar Reynolds numbers. The axial velocity profiles for the Newtonian fluid are obtained through numerical simulation using the Navier–Stokes equations

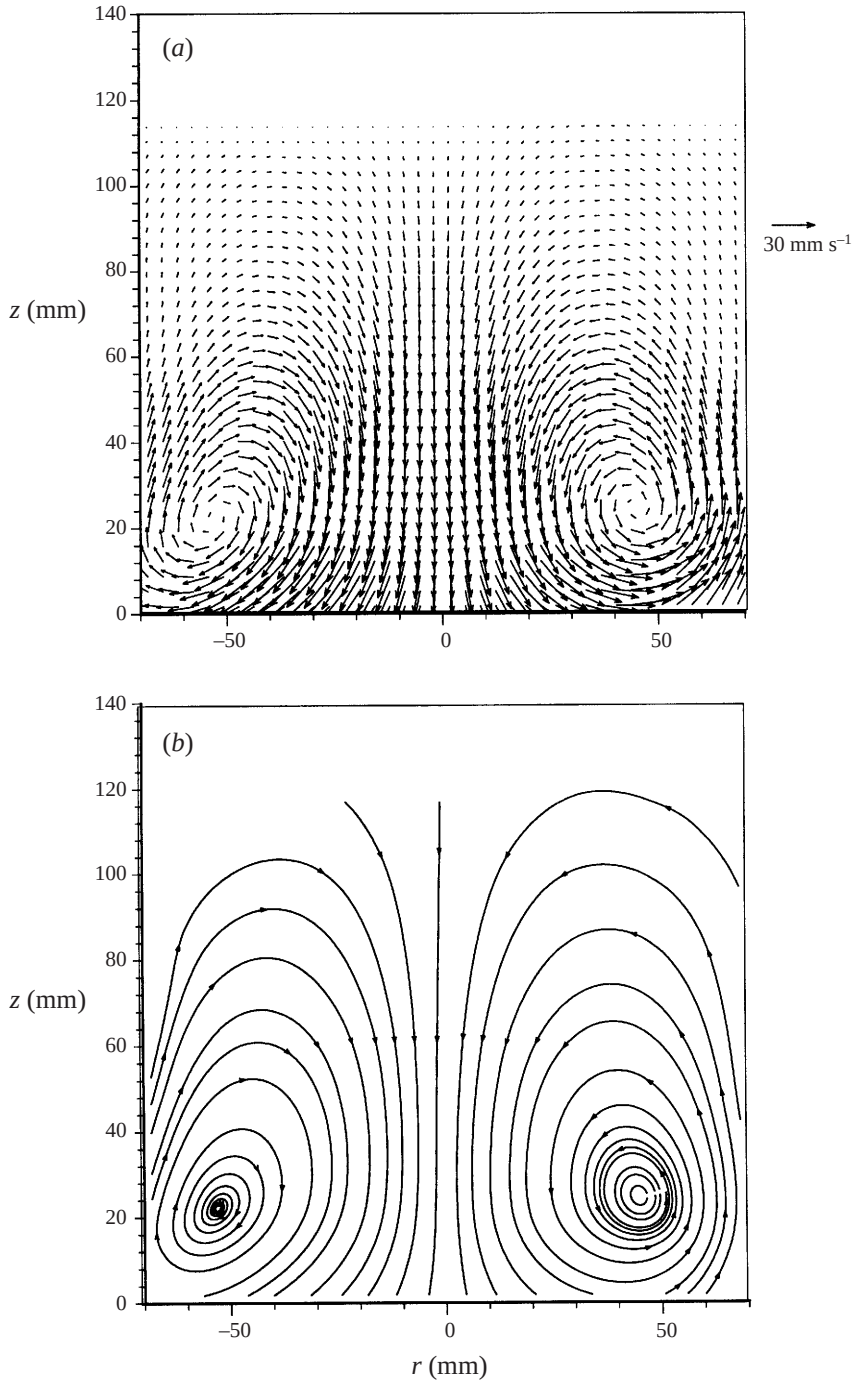

FIGURE 7(*a*, *b*). For caption see facing page.

(Brydon & Thompson 1998; Brydon personal communication 1998). The Newtonian profiles show a slight decrease in the minimum axial velocity peak with increase in Reynolds number with the minimum occurring at increasing values of the cylinder aspect ratio. However, the peak axial velocity distribution for polyacrylamide fluid

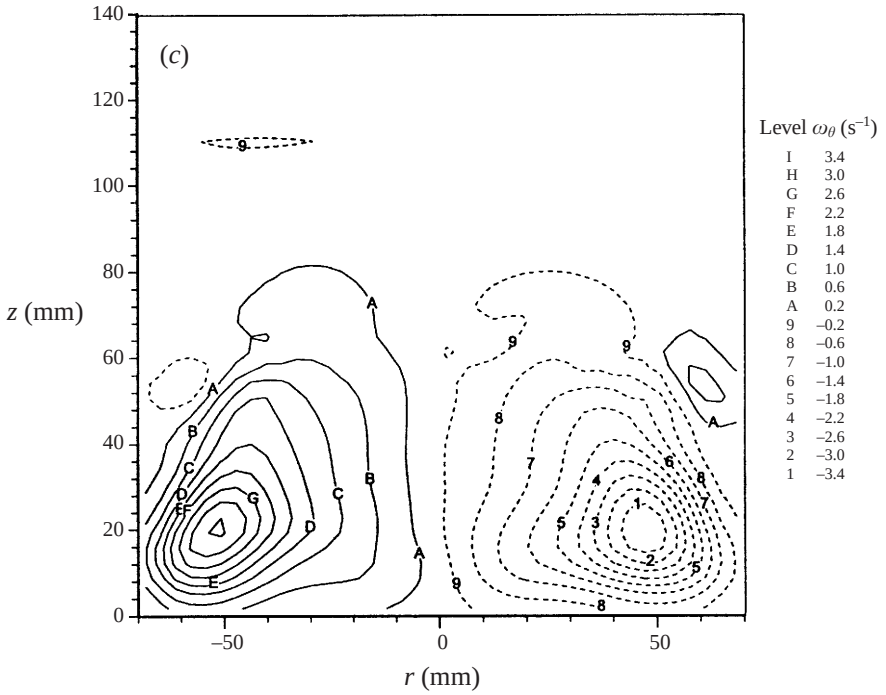

FIGURE 7. Particle image velocimetry results in the secondary flow plane for polyacrylamide fluid A showing steady 'Newtonian-like' flow at $Re = 216$, $We = 0.05$ and $H/R = 2$ indicating (*a*) vector field, (*b*) sectional streamline patterns, and (*c*) azimuthal vorticity contours.

A does not follow the same progression as the Newtonian fluid. The minimum velocity occurs essentially at a constant value of aspect ratio ($0.35 < H/R < 0.5$) and the minimum velocity initially decreases in value with increasing Reynolds number, and then increases in value. The lowest peak axial velocity measured for the results presented in figure 9 is for a Reynolds number of $Re = 280$ ($We = 0.065$), above which the minimum velocity increases. Asymmetry in the flow is detected at a Reynolds number of $Re = 300$ which is at the same point as the minimum velocity increase. Although an asymmetry is present for $Re > 300$, and a flow instability occurs at $Re = 380$, the velocity distributions shown in figure 9 represent a combination of two to four PIV images resulting in a 5–10% variation in the measurements owing to the transient nature of the flow. In the case of $Re = 570$, the peak axial velocity is approximately 25% lower in magnitude than for the Newtonian case at a similar Reynolds number. These results are also consistent with those in Part 1 where a reduction in the magnitude of the axial velocity minimum results, owing to the influence of elasticity at high Reynolds numbers for low-viscosity Boger fluids. The increase in minimum axial velocity at $Re > 300$ is due to increased effects of fluid elasticity and also associated with the occurrence of the instability at $Re = 380$.

Axisymmetric vortex breakdown is not observed for polyacrylamide fluid A for Reynolds numbers as high as $Re \approx 3000$. This is expected, considering breakdown was suppressed when using 75 p.p.m. polyacrylamide, as described in Part 1. Fluid A is also susceptible to severe degradation at high rotation rates when $Re > 1000$. The degraded fluid is replaced with fresh fluid when this occurred. It is also noted that when the rotating lid is continually operated for over about an hour at moderate

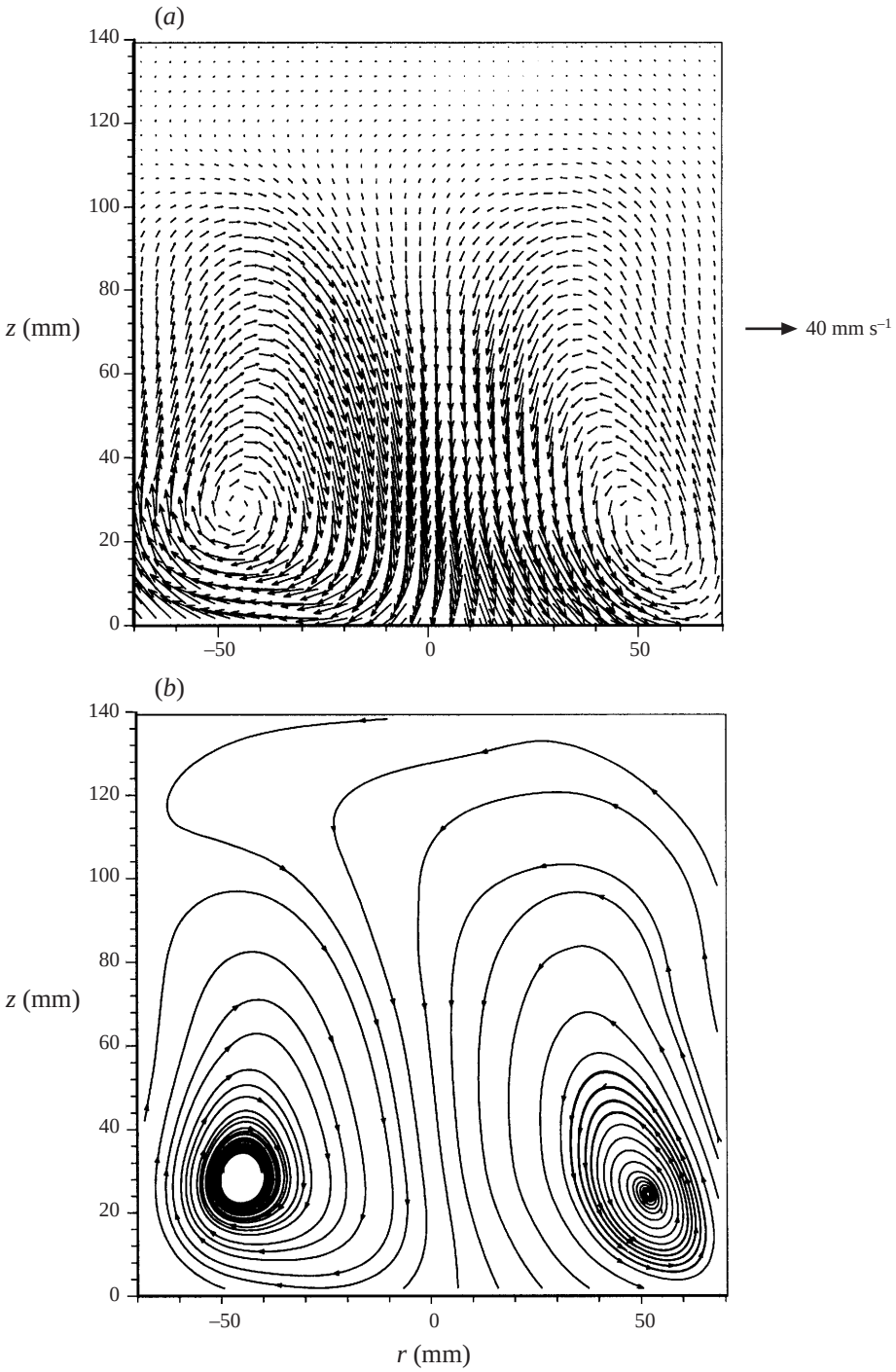

FIGURE 8(*a*, *b*). For caption see facing page.

rotation rates ($200 < Re < 600$), the critical Reynolds number for the instability increases from $Re = 380$ to as high as $Re \approx 550$ in some cases. The temperature of the fluid did not change significantly and, hence, this apparent increase in critical Reynolds number is not associated with viscous heating. However, when the rotation

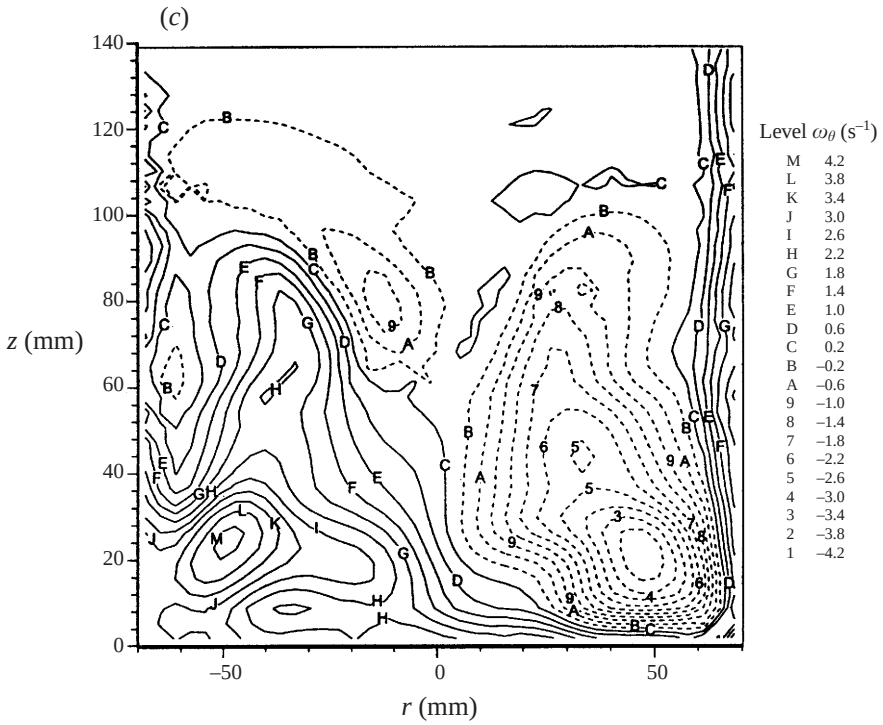

FIGURE 8. Particle image velocimetry results in secondary flow plane for polyacrylamide fluid A for the onset of unsteady flow at $Re = 378$, $We = 0.089$ and $H/R = 2$ indicating (*a*) vector field, (*b*) sectional streamline patterns, and (*c*) azimuthal vorticity contours.

is stopped and the fluid remains still for several hours, the critical Reynolds number for the instability is once again initially found to be about $Re = 400$. Hence, this indicated that the fluid had not degraded and at present the mechanism for this phenomenon is unclear.

The secondary flow for polyacrylamide fluid B, which had an elasticity number of $El = 0.002$ (an order of magnitude above that for fluid A), is steady and 'Newtonian-like' at Reynolds numbers of $Re < 78$ ($We < 0.14$), as shown in figure 10(*a*). The transformation to an unsteady flow state and a complex flow field took place at $Re = 78$ with the resulting flow field illustrated in figure 10(*b*) with a dye flow-visualization image presented in figure 10(*c*). When the disk rotation rate is increased to the critical value for the unsteady flow field, 'Newtonian-like' flow is initially observed. After one to two minutes, the fluid in the top half of the cylinder becomes stagnant before a jet of fluid travels upwards from the centre of the rotating disk. This jet of fluid becomes a slow spiralling vortex travelling upwards from the central region of the disk. The initial 'Newtonian-like' vortex is reduced in size to 25–50% of the cylinder height and is situated in the lower half of the cylinder near the edge of the rotating disk. The flow in the top half of the cylinder is in the 'reverse' direction and driven by elastic effects. A small ring vortex near the centre of the disk is also apparent and flows in the inertial direction. The overall flow field after several minutes resembles the illustration shown in figure 10(*b*) with a dye streak-line image presented in figure 10(*c*).

The highly complex flow field restricted velocity measurements for polyacrylamide fluid B to steady and 'Newtonian-like' conditions. Axial velocity measurements along

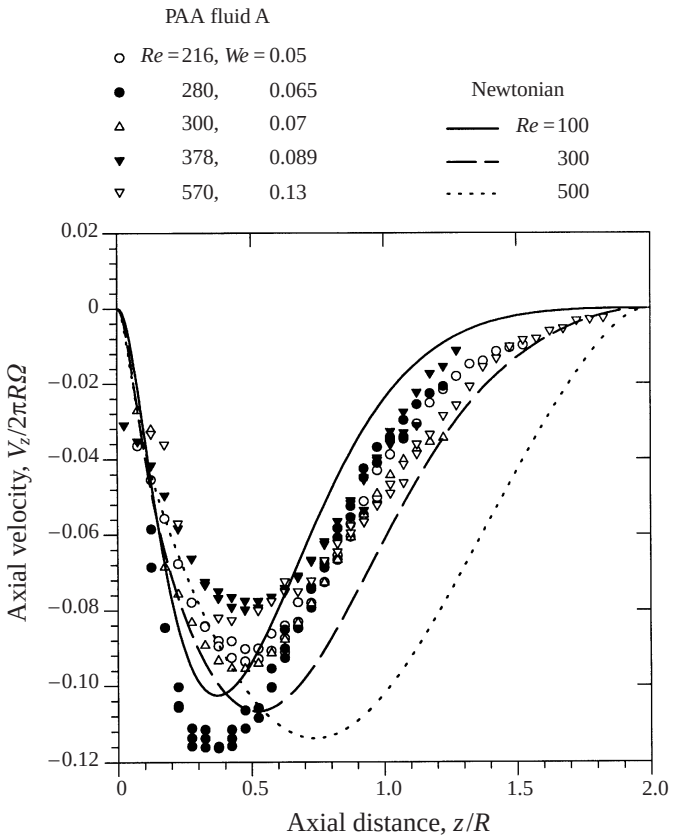

FIGURE 9. Dimensionless axial velocity profiles along the central axis ($r \approx 0$) for polyacrylamide fluid A at $H/R = 2$. Also shown is the predicted axial velocity profiles for a Newtonian fluid (Brydon personal communication 1998).

the central axis are presented in figure 11 for fluid B with a comparison to the velocity predicted for Newtonian fluids (Brydon personal communication 1998). The minimum in axial velocity for fluid B is about 20% smaller in magnitude than for Newtonian fluids, but the peak velocity occurs at essentially the same aspect ratio.

The results at this stage, using low-viscosity (Part 1) and medium-viscosity Boger fluids (polyacrylamide fluids A and B), suggest that, even in inertia-dominated flows, elasticity can have a large affect on the flow kinematics. For low values of elasticity number ($El < 0.002$), the effect of elasticity is to decrease the secondary flow circulation initially. The flow fields for the polyacrylamide fluids A and B, which are flexible polymer Boger fluids, are initially Newtonian-like at low Reynolds numbers, but become highly unsteady when the rotation rate of the disk is increased, such that a critical combination for the Reynolds and Weissenberg (or elasticity) numbers is reached. From this initial work, the unsteady flow fields produced are thought to be a direct result of fluid elasticity and/or due to the competition between inertia and elastic forces.

3.2. *Elasticity dominated flow of flexible polymer Boger fluids*

The confined swirling flow of elastic fluids where inertia is less dominant and the flow is governed primarily by viscous and elastic forces, is examined using polyacrylamide

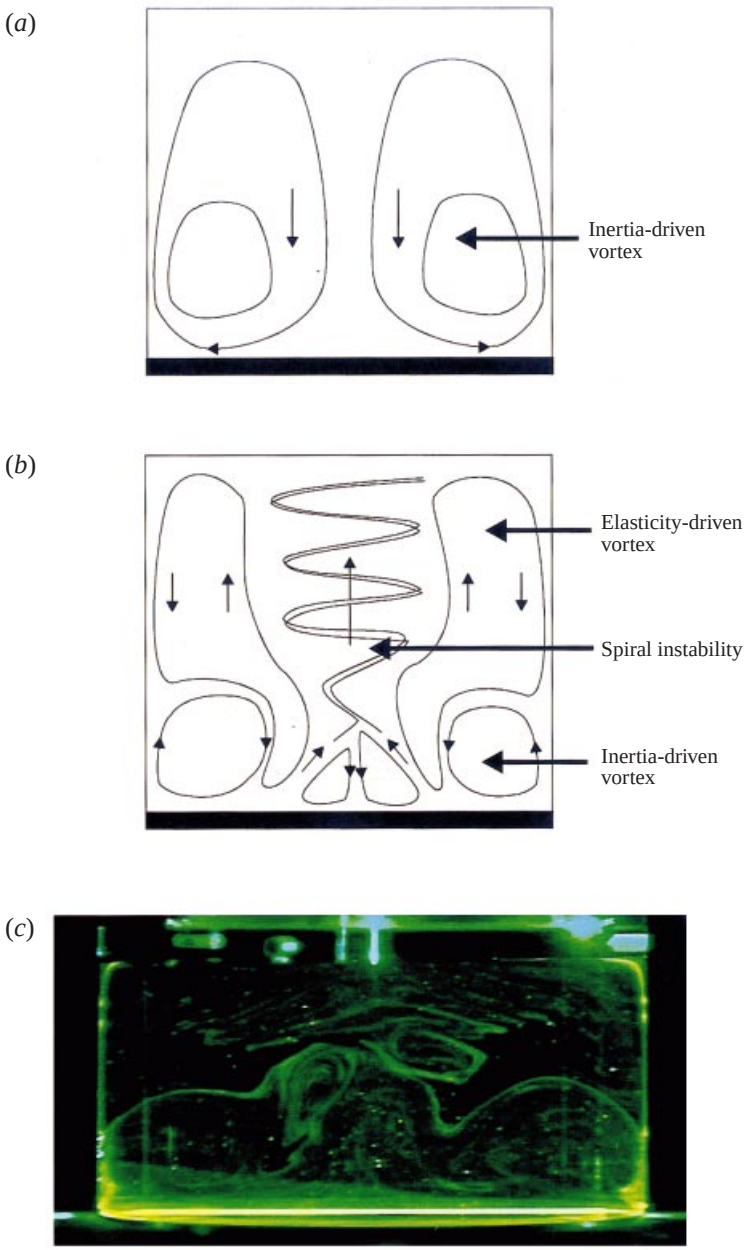

FIGURE 10. Representation of secondary flow field for polyacrylamide Boger fluid B indicating (*a*) 'Newtonian-like' flow at $Re \approx 77$, $We \approx 0.15$, (*b*) unsteady flow at $Re = 83$, $We = 0.17$ and (*c*) flow-visualization video image of instability for $H/R = 1$ at $Re = 83$, $We = 0.17$.

fluids C, D and E with elasticity numbers of $El = 0.05, 0.17$ and 10, respectively. In what follows, elasticity is observed to dominate the flow for all three Boger fluids such that the secondary flow is radially inwards along the rotating lid and against the centrifugal force. Once a critical combination of Reynolds number and Weissenberg number (or elasticity number) is reached, it will be shown that a three-dimensional instability is created and the flow becomes highly unsteady. The various secondary

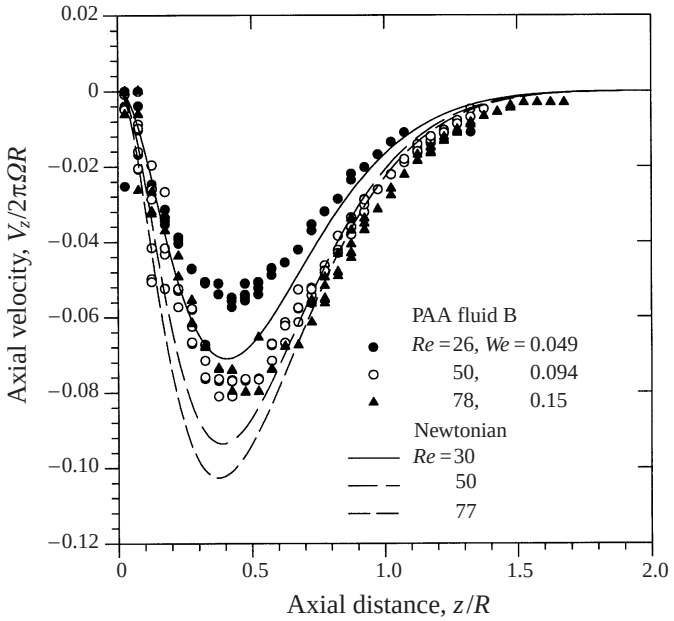

FIGURE 11. Dimensionless axial velocity along the central axis ($r \approx 0$) for polyacrylamide fluid B for $H/R = 2.0$. Also shown is the predicted axial velocity profiles for a Newtonian fluid (Brydon personal communication 1998).

flow states of fluid C are initially examined using streak photographs and pictorial illustrations. Fluorescent dye flow-visualization images of fluid D are then used to illustrate the instability, which is similar for all three high-viscosity Boger fluids. Velocity fields obtained using PIV for polyacrylamide fluids C and E with the axial velocity along the centreline are also used to examine the effect of the instability on the secondary-flow circulation rates.

Streak photographs and a pictorial representation of the secondary flow for the transition between different flow structures of polyacrylamide fluid C at an aspect ratio of $H/R = 2$ are shown in figure 12. The secondary flow for polyacrylamide fluid C at low Reynolds numbers ($Re < 1.88$, $We < 0.085$) is in the 'reverse' direction where elastic forces dominate (figure 12*a*). 'Reverse' flow is caused by the uneven normal stresses (τ_{rr} τ_{00} τ_{zz}) induced in the fluid near the rotating lid. These normal stresses create a tension along the primary flow streamlines with a resultant force directed radially inwards and opposite to centrifugal forces. When the normal stresses are large, as in the case of fluids C, D and E, the fluid is driven radially inwards in the opposite direction to that for a Newtonian fluid. An increase in rotation rate ($Re = 6.2$, $We = 0.28$) for fluid C produces a weakly driven ring vortex on the centre of the disk which flows in the inertial direction (figure 12*b*). A spiral instability is produced at $Re = 6.9$ ($We = 0.31$) where the core vortex spirals with the primary motion of fluid and the secondary flow field takes on a wavy appearance (figure 12*c*). The counter-rotating vortex on the centre of the disk then disappears with further increases in rotation rate ($Re = 11$, $We = 0.5$) and the flow becomes highly unsteady (figure 12*d*).

Flow visualization images using fluorescent dye to show the elasticity driven 'reverse' flow and the spiral instability are presented in figure 13 using polyacrylamide fluid D with $t = 0$ corresponding to the start-up of the rotating disk. The images presented

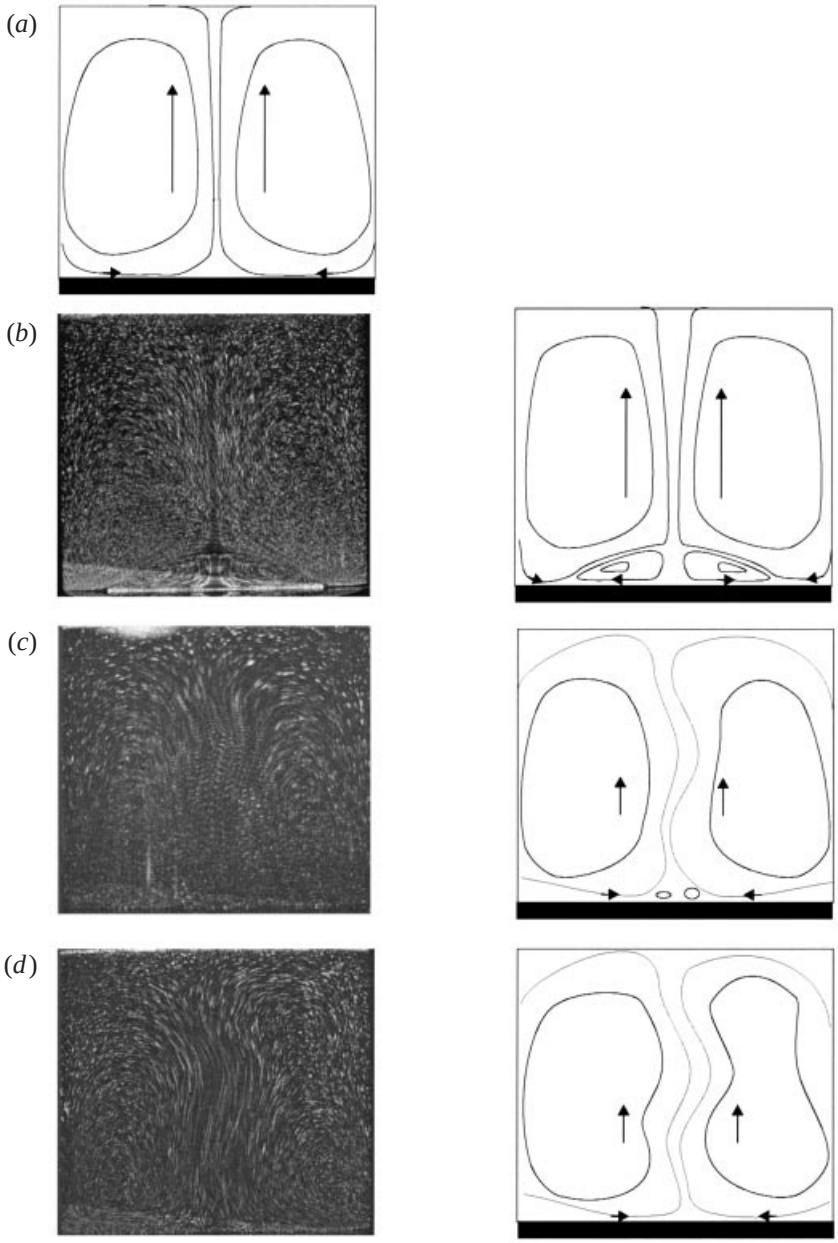

FIGURE 12. Streak photographs and corresponding pictorial representation of secondary flow field for the elasticity dominated flow of polyacrylamide fluid C at $H/R = 2$ indicating (*a*) 'reverse' flow at $Re = 1.88$, $We = 0.085$, (*b*) central ring vortex at $Re = 6.15$, $We = 0.28$, (*c*) instability and central ring vortex at $Re = 6.9$, $We = 0.31$, and (*d*) instability at $Re = 11$, $We = 0.5$.

are for an aspect ratio of $H/R = 1.8$, while images at an aspect ratio of $H/R = 1$ can be found in Stokes *et al.* (1995) and Stokes (1998). The flow kinematics are similar to those observed for fluid C except that a counter-rotating ring vortex on the centre of the disk is not observed under steady-flow conditions for fluid D. Figure 13(*a*) shows the 'reverse' secondary flow of fluorescent dye for $Re = 1.97$ ($We = 0.19$). When the

(*a*)

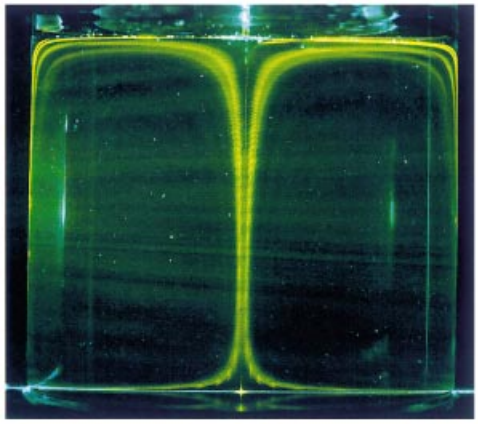

(*b*)

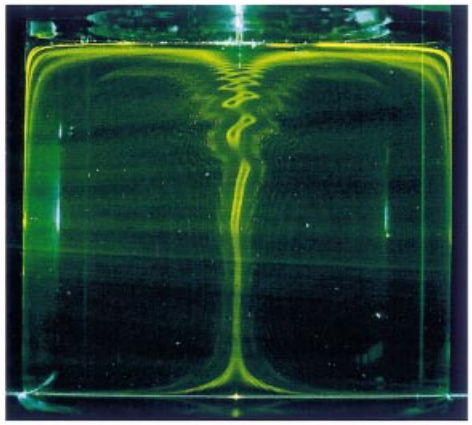

$t = 150$ s

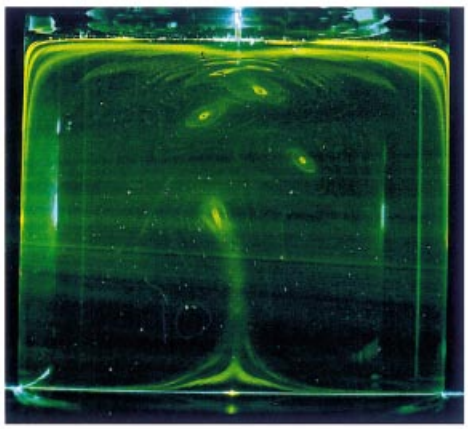

$t = 185$ s

FIGURE 13(*a*, *b*). For caption see facing page.

(*b*, *contd.*)

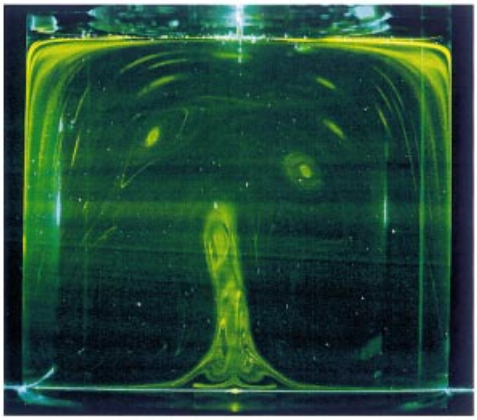

$t = 340$ s

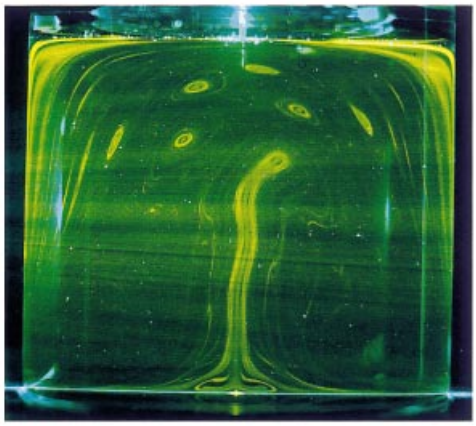

$t = 400$ s

(*c*)

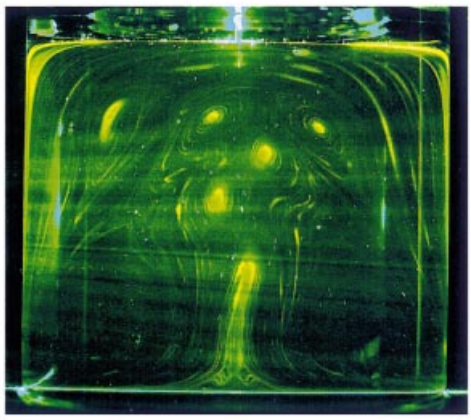

FIGURE 13. Dye flow-visualization images for the secondary flow of polyacrylamide fluid D at $H/R = 1.8$ indicating (*a*) 'reverse' flow at $Re = 0.313$, $We = 0.03$, (*b*) development of spiral instability at $Re = 0.57$, $We = 0.054$ at the indicated times after start-up, and (*c*) spiral instability at $Re = 0.913$, $We = 0.067$

rotation rate is increased such that $Re = 3.6$ ($We = 0.34$), the flow becomes unsteady with the development of a spiral instability shown in figure 13(*b*) for a sequence in time. Initially, after about 150 s from the start-up of the rotating disk to the critical rate, the core of the primary vortex takes on a wavy shape and begins to spiral near the stationary lid. The wave progressed down towards the rotating lid against the axial flow direction and the amplitude increases as the core begins to spiral in a three-dimensional manner with the primary vortex motion ($t = 185$ s). A small counter-rotating vortex then forms on the middle of the rotating lid and is driven in the inertial direction ($t = 340$ s). Dye is drawn occasionally upwards from the centre of the disk, despite the presence of the small inertial ring vortex which attempts to drive the dye in the opposite direction. The counter-rotating vortex disappears with further increases in Reynolds number as the flow becomes more chaotic (figure 13*c*).

In all the Boger fluids used in this work, the period of the spiral instability is not discernible, so that it appeared to behave in a chaotic manner. However, for the slightly shear-thinning fluid, fluid Fst, a period for the spiralling motion is detectable which appeared to be dependent on the rotation rate of the disk. Details on the rheological properties for fluid Fst may be found in Stokes (1998). As shown in figure 13 for polyacrylamide fluid D, the instability appears similar to vortex shedding as the core vortex spirals around with the primary motion of the fluid. The period (Γ) for a complete revolution of the core, which also corresponds to the appearance of three vortices being 'shed', for the shear-thinning fluid Fst is given by: $\Gamma \approx 2.9/\Omega$. Other polyacrylamide fluids tested do not appear to have this characteristic and the mechanisms are currently unclear. However, it does suggest that perhaps there is a regular period for the 'shedding' of vortices for the Boger fluids but further work is required to examine this characteristic in more detail.

Instantaneous velocity measurements were made using PIV for polyacrylamide fluid C in the presence of the spiral instability with the resulting vector diagram and sectional streamline plot shown in figures 14(*a*) and 14(*b*) for an aspect ratio of $H/R = 2$ at $Re = 11.5$ ($We = 0.52$). An axial velocity contour plot is shown in figure 14(*c*), indicating a central region where the axial velocity reaches as maximum of around 21 mm s^{-1}, and the azimuthal component of vorticity is displayed in figure 14(*d*). These diagrams show asymmetry in the flow field which is due to the presence of the instability and transient flow behaviour. The vorticity diagram in figure 14(*d*) shows an area of positive azimuthal vorticity on the left-hand side of the flow field which is otherwise dominated by negative azimuthal vorticity. The area of near zero vorticity along the central axis, and bounded by positive and negative azimuthal vorticity, may be regarded as the core vortex which is spiralling from the centre of the rotating disk. The core vortex is, therefore, shown in this case to be situated to the left-hand side of the flow cell for $z \approx 100$ mm such that there is an area of positive vorticity above the core region in the left-side of figure 14(*d*). Figure 14(*e*) shows the instantaneous azimuthal vorticity contour plot for an aspect ratio of $H/R = 1$, also for the case of when a spiral instability was present. The core region of near zero vorticity is slightly wavy, but only vorticity of the same sign is found in each half of the figure in this case.

The spiral instability is also found to occur for polyacrylamide fluid E, which is the most viscous and elastic Boger fluid used in this work, for Reynolds numbers much less than unity such that inertia is completely negligible. 'Reverse' flow is observed at very low Reynolds numbers until the instability occurs at $Re = 0.088$ ($We = 0.82$) with a small counter-rotating ring vortex on the centre of the disk similar to that observed for fluid D in figure 13(*b*). However, the ring vortex disappears over an

extended period of time for fluid E ($t \approx 30$ min). Figure 15 shows an instantaneous vector map in the presence of the spiral instability with contour diagrams of the axial velocity and azimuthal vorticity. In contrast to the axial velocity counter plot for fluid C in figure 14(*c*), the areas of maximum axial velocity are no longer found along the central axis but are found on either side of the vertical axis for fluid E, as shown in figure 15(*b*) at $r \approx \pm 15$ mm. The azimuthal vorticity contour plot for fluid E in figure 15(*c*) is also different from those found for fluid C in figures 14(*a*) and 14(*e*). Five cores of negative azimuthal vorticity are observed in figure 15(*c*) with two of these cores situated on the right-hand side of the flow cell which is otherwise dominated by large areas of positive vorticity. The contours of azimuthal vorticity on both the left- and right-hand sides of figure 15(*c*) are essentially mirrors of each other, except that they are of opposite sign.

The axial velocity along the centreline ($-5\,\text{mm} < r < 5\,\text{mm}$) for polyacrylamide fluid C at two aspect ratios, $H/R = 1$ and $H/R = 2$, is shown in figure 16. Each Reynolds number shown corresponds to the images presented in figure 12. The velocity distributions shown for $Re \geqslant 7.5$ were obtained by averaging the velocity distributions from 3 to 5 PIV images at different pulse separation times from the transient flow field. From this data, the axial velocity is found to fluctuate by as much as $\pm 50\%$ from the mean velocity. At low Reynolds numbers where only steady 'reverse' flow is present ($Re \leqslant 6.0$, $We \leqslant 0.27$), the axial velocity reaches a maximum of $V_Z/2\pi R\Omega \approx 0.012$. When the flow becomes unsteady with a small increase in Reynolds number to $Re = 7.5$ ($We = 0.34$), there is an increase in the maximum velocity by more than 400%, indicating that the secondary flow increases significantly in strength as a result of the instability. The maximum axial velocity only increases slightly more for an increase in Reynolds number to $Re = 11.5$ ($We = 0.52$) when $H/R = 1$, as shown in figure 16(*a*), but increases by 200% for $H/R = 2$ to a maximum of $V_Z/2\pi R\Omega \approx 0.1$, as shown in figure 16(*b*). The maximum axial velocity along the centreline in this case is 10% of the maximum azimuthal velocity at the edge of the rotating disk and is of the same order of magnitude as that observed for the high-Reynolds-number flow ($Re > 100$) of Newtonian fluids, but of opposite sign. The flow in the presence of the instability may be classed as quite strong and the unsteady nature of the flow indicates good mixing capabilities. The stationary wall suppresses the peak velocity at low aspect ratios and hence a 170% greater peak axial velocity is observed for $H/R = 2$ than for $H/R = 1$ at $Re = 11.5$.

The centreline axial velocity for polyacrylamide fluid E is presented in figure 17 for $H/R = 1$. Steady 'reverse' flow is observed for $Re = 0.044$ ($We = 0.41$) with a peak axial velocity of $V_Z/2\pi R\Omega \approx 0.034$ which is 280% larger than the peak axial velocity for the reverse flow of fluid C owing to the higher elasticity of fluid E. However, a 170% increase in peak axial velocity is observed for fluid E when the Reynolds number is increased to that required for the spiral instability at $Re = 0.089$ ($We = 0.82$). Further increases in Reynolds number to $Re = 0.35$ ($We = 3.2$) for fluid E in figure 17 results in an increase in peak axial velocity to $V_Z/2\pi R\Omega \approx 0.108$.

The previous results have, therefore, shown that in the elasticity dominated flow of polyacrylamide Boger fluids, normal stress effects drive the fluid in the opposite direction to that in which the inertial forces act such that the flow is moving inwards along the rotating lid. A small counter-rotating ring vortex driven in the inertial direction forms on the centre of the rotating lid with Reynolds numbers being well below one in some cases. The formation of a central ring vortex is not unexpected, however, since it is qualitatively predicted theoretically by Kramer & Johnson (1972), Nirschl & Stewart (1984) and Signer (1991) for constant viscosity fluids with moderate

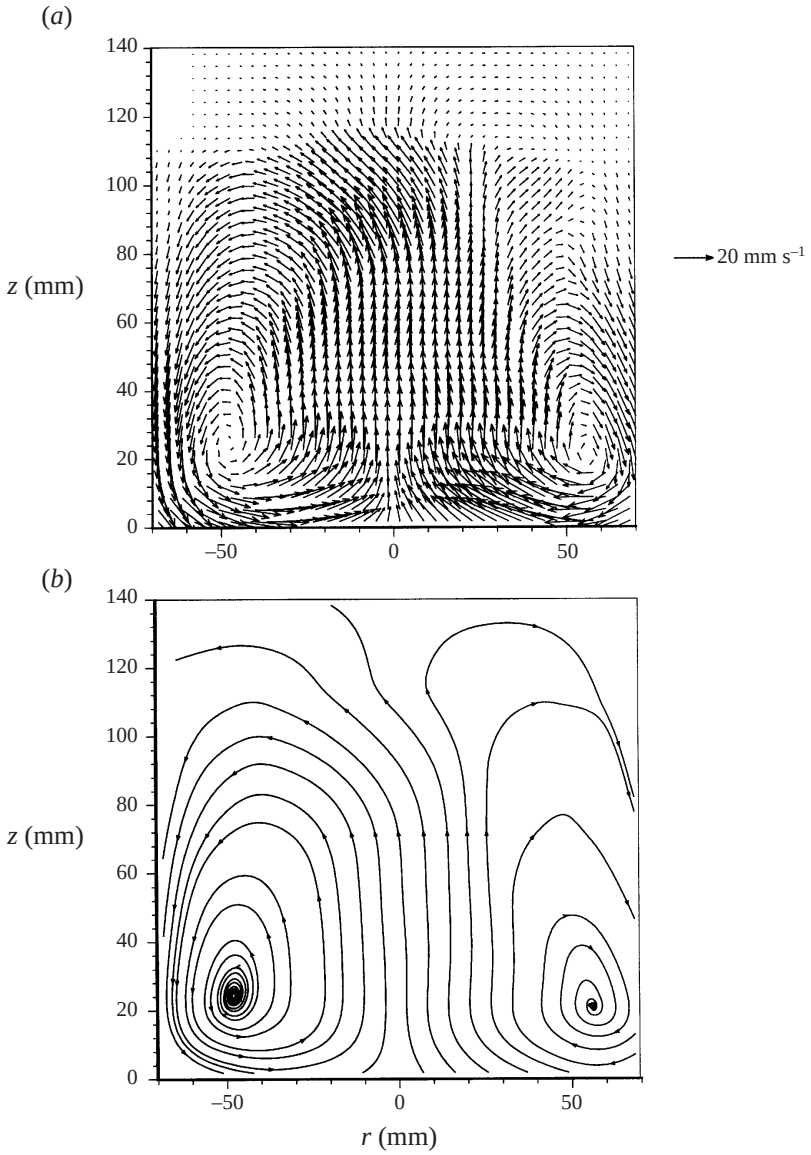

FIGURE 14(*a*, *b*). For caption see facing page.

amounts of elasticity. This is contrary to the experimental observations of Hill (1972) where an inertially driven ring vortex forms on the outside of the rotating lid and is associated with the action of shear thinning. Beyond a critical combination of Reynolds and Weissenberg (or elasticity) numbers, the core vortex is shown to become a three-dimensional spiral and the flow is highly unsteady with a substantially increased secondary-flow circulation rate.

3.3. *Elasticity dominated flow of a semi-rigid polymer Boger fluid*

The following will illustrate the confined swirling flow of a xanthan gum Boger fluid when inertial forces are small. Xanthan gum has a semi-rigid conformation in solution and has substantially different rheological properties compared to the

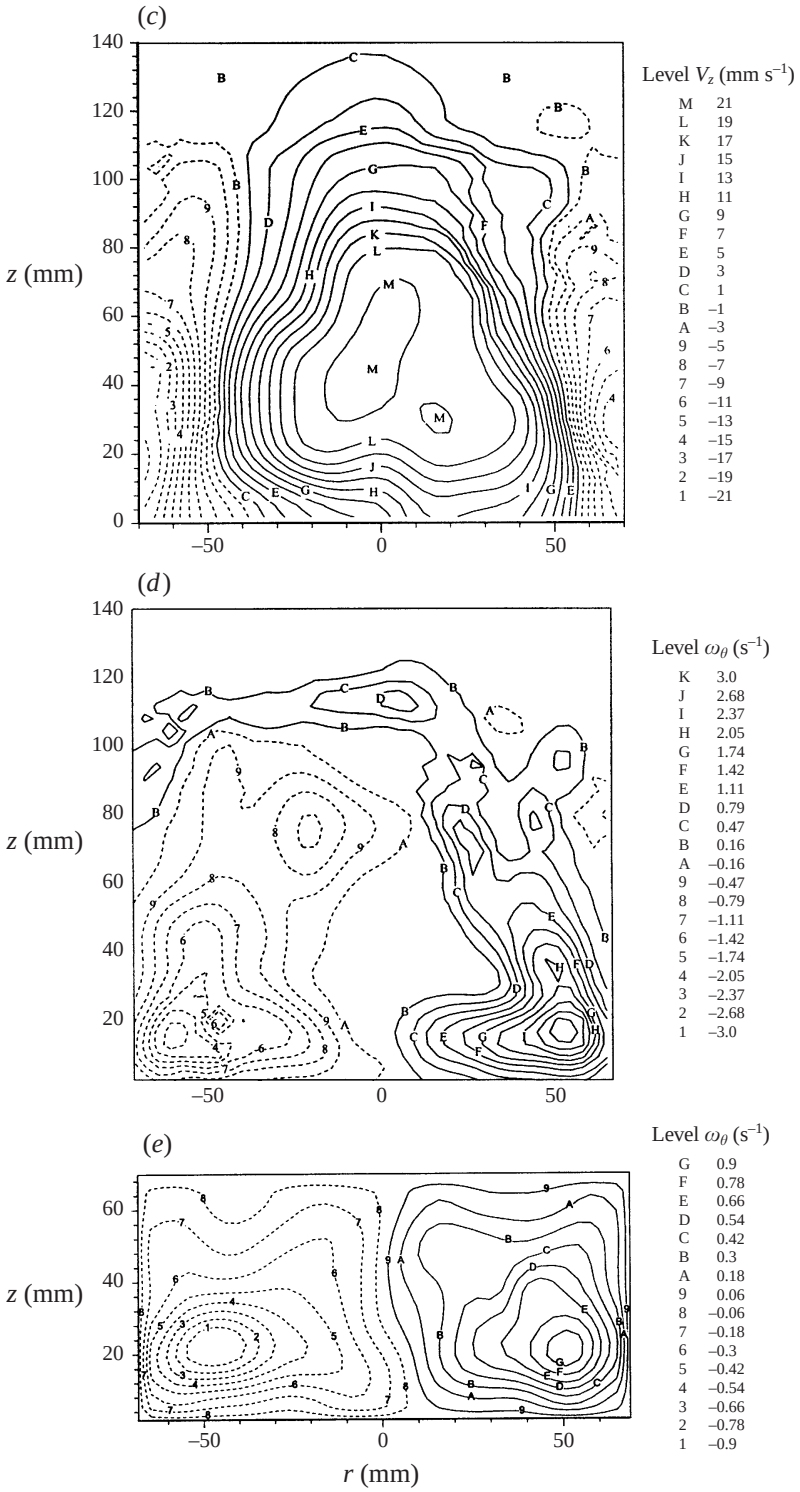

FIGURE 14. Particle image velocimetry results in secondary flow plane for polyacrylamide fluid C in the presence of an instability at $Re = 11.5$, $We = 0.52$, and $H/R = 2.0$ indicating (*a*) vector field, (*b*) sectional streamline patterns, (*c*) axial velocity contour plot, (*d*) azimuthal vorticity contour plot, and (*e*) azimuthal vorticity contour plot for $H/R = 1$.

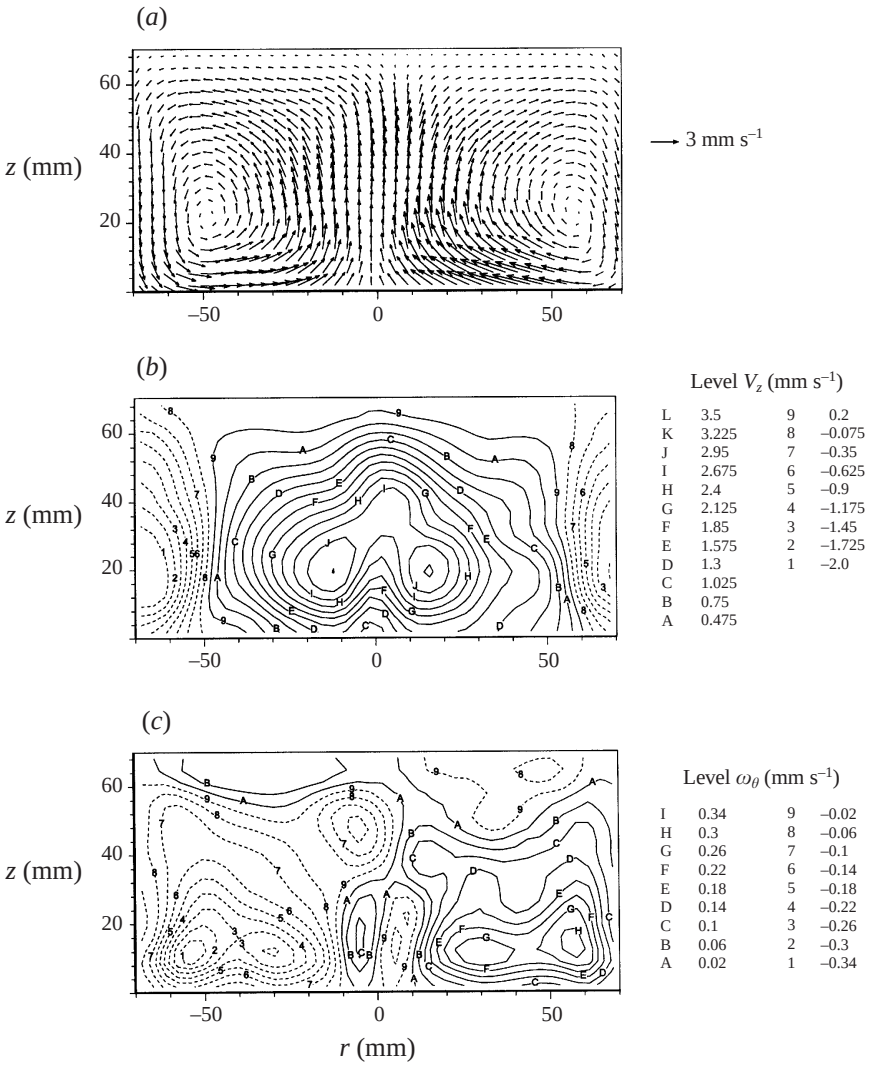

FIGURE 15. Particle image velocimetry results in secondary flow plane for polyacrylamide fluid E in the presence of an instability at $Re = 0.088$, $We = 0.88$ and $H/R = 1.0$ indicating (*a*) vector field, (*b*) axial velocity contour plot, (*c*) azimuthal vorticity contour plot.

flexible polyacrylamide solutions used in the previous two sections. The following results show that the flow kinematics for the xanthan gum solution are also quite different to those for the polyacrylamide solution as a result of the differences in rheology. The relaxation time for the xanthan gum Boger fluid also decreases with increasing rotation rate (or shear rate) and, hence, the Weissenberg and elasticity numbers correspondingly decrease as the Reynolds number is raised. However, in all cases for the xanthan gum Boger fluid, $Re < 1.3$ and $El > 0.8$, indicating that it is expected that elasticity dominates over the inertial forces. The following results show that elastic driven 'reverse' flows are observed at low Reynolds numbers and high Weissenberg numbers for the xanthan gum Boger fluid. Ring vortices are also observed on the rotating disk driven in the inertial direction and depend on the cylinder aspect ratio. Figure 18 and 21 are streak photographs and a pictorial representation for the

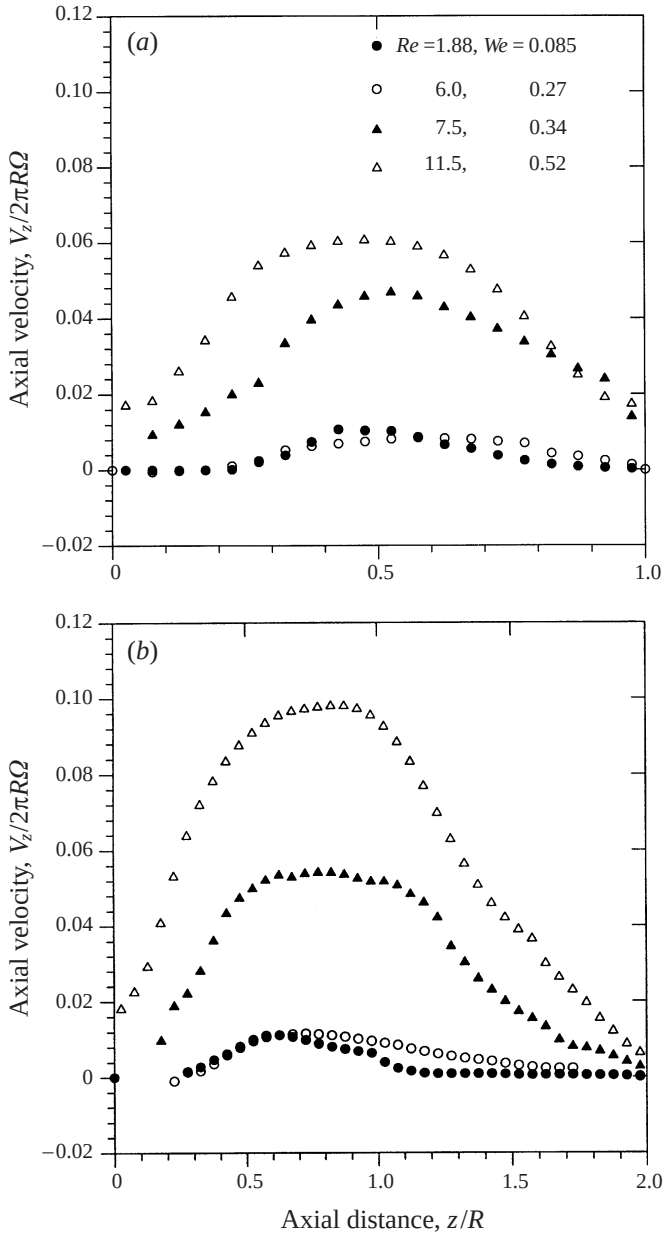

FIGURE 16. Dimensionless axial velocity along central axis ($r \approx 0$) for polyacrylamide fluid C for (*a*) $H/R = 1.0$ and (*b*) $H/R = 2$.

secondary flow of the xanthan gum Boger fluid at an aspect ratio of $H/R = 1.0$ and $H/R = 1.5$, respectively, and these results are now discussed in more detail.

At an aspect ratio of $H/R = 1$, the xanthan gum Boger fluid exhibits elastic 'reverse' flow at Reynolds numbers of $Re \leqslant 0.25$ ($We \geqslant 4.2$) as shown in figure 18(*a*). On increasing the Reynolds number to $Re = 0.59$ ($We = 2.8$, figure 18*b*), a small ring vortex, which is driven in the inertial direction, forms on the outside of the rotating disk and counter-rotates with the elastic vortex. The ring vortex grows to govern just

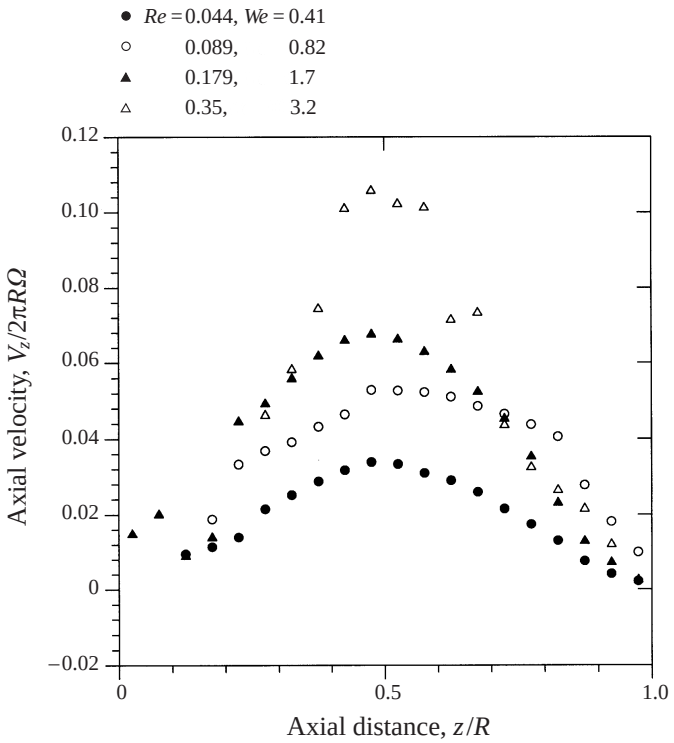

FIGURE 17. Dimensionless axial velocity along central axis ($r \approx 0$) for polyacrylamide fluid E for $H/R = 1.0$.

under half of the flow cell at the highest Reynolds number tested ($Re = 1.3$, $We = 2$, figures 18*c*, 18*d*). The area near the centre of the disk appears almost stagnant and is only moving slowly downwards towards the disk at a velocity of approximately 0.1% of the maximum azimuthal velocity at the edge of the rotating disk.

At the higher aspect ratio of $H/R = 1.5$, a small weakly flowing ring vortex driven in the inertial direction forms on the centre of the rotating disk at an $Re = 0.12$ ($We = 5.7$, figure 19*b*). Another small ring vortex also forms on the outside of the disk at $Re = 0.36$ ($We = 3.5$, figure 19*c*), which is similar to that observed for $H/R = 1$. The two vortices combine at $Re = 0.48$ ($We = 3.0$, figure 18*d*) to form one deformed ring vortex on the disk. A weak instability is also observed near the stationary disk, shown in figure 19 as a slight asymmetry.

The dimensionless axial velocity along the centreline for the xanthan gum Boger fluid is shown in figure 20 at each aspect ratio. The dimensionless axial velocity peak is of equal order of magnitude to that observed for the steady 'reverse' flow of polyacrylamide fluid C. However, as the Reynolds number is increased and the Weissenberg number decreased, the peak axial velocity decreased. This decrease in peak velocity is in contrast to the polyacrylamide Boger fluid where the peak axial velocity is observed to increase with increasing Reynolds number and Weissenberg number. The slight instability observed for the xanthan gum fluid at $H/R = 1.5$ has no noticeable effect on the axial velocity distribution along the central axis, and, hence, this instability is considered to be weak in nature.

The results have shown that the secondary flows observed for the xanthan gum Boger fluid are considerably different to those observed for polyacrylamide Boger

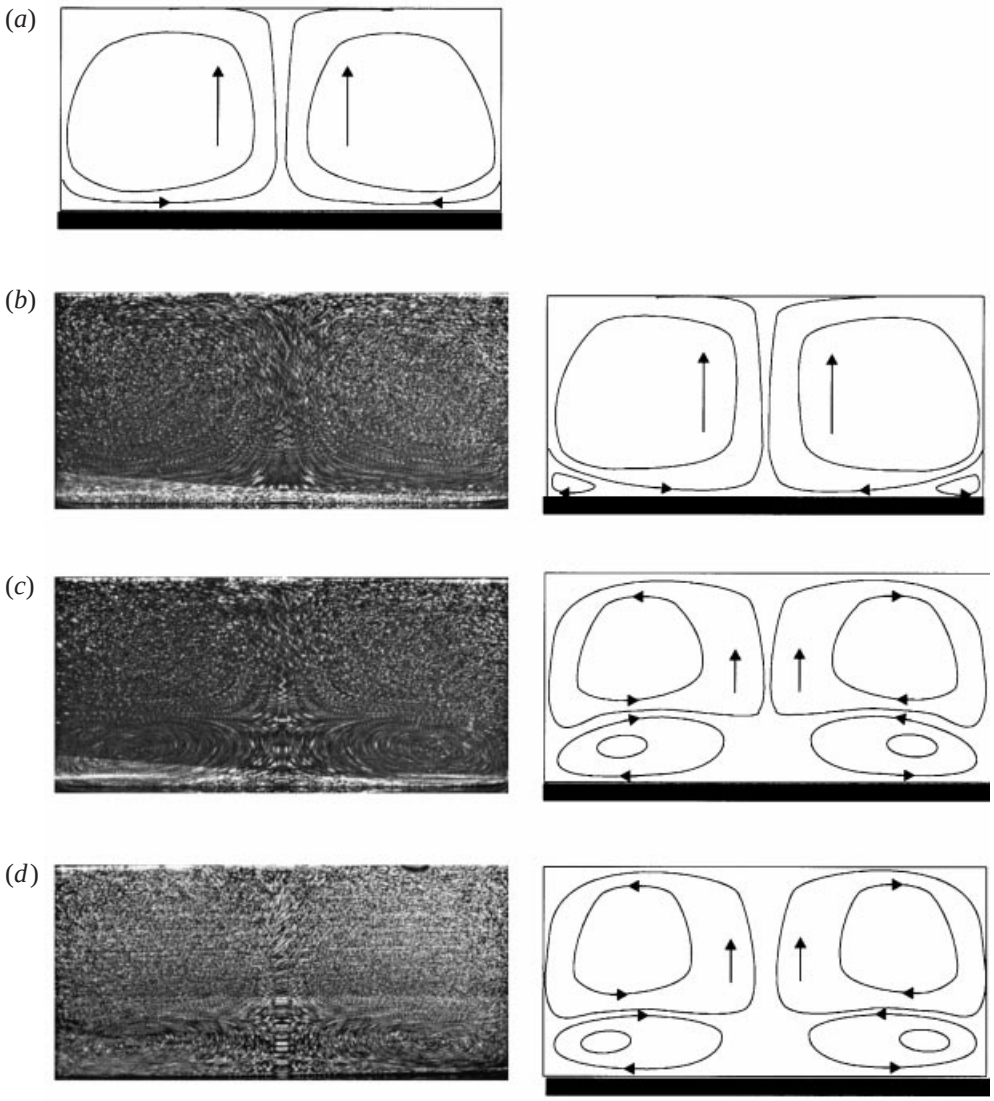

FIGURE 18. Streak photographs and pictorial representation of a xanthan gum Bogar fluid for $H/R = 1.0$ showing (*a*) 'reverse' flow at $Re = 0.25$, $We = 4.2$, (*b*) small outside ring vortex at $Re = 0.59$, $We = 2.8$, (*c*) ring vortex at $Re = 0.94$, $We = 2.2$, and (*d*) ring vortex at $Re = 1.3$, $We = 2$.

fluids. Ring vortices are observed on both the outside and in the centre of the disk, depending on the aspect ratio of the cylinder. The reason for the formation of a central ring vortex at $H/R = 1.5$ is thought to be due to the creation of a low-pressure region in the centre of the disk, and is similar to the ring vortex observed for the high-viscosity polyacrylamide Boger fluids. The ring vortex observed on the outside of the disk for the xanthan gum fluid is also thought to be created by a low-pressure region in the bottom corners of the flow cell in the area of the singularity between the rotating disk and the stationary wall. Outside ring vortices were previously observed experimentally by Hill (1972) and Escudier & Cullen (1996) but are associated with shear thinning, while for the xanthan Boger fluid the viscosity

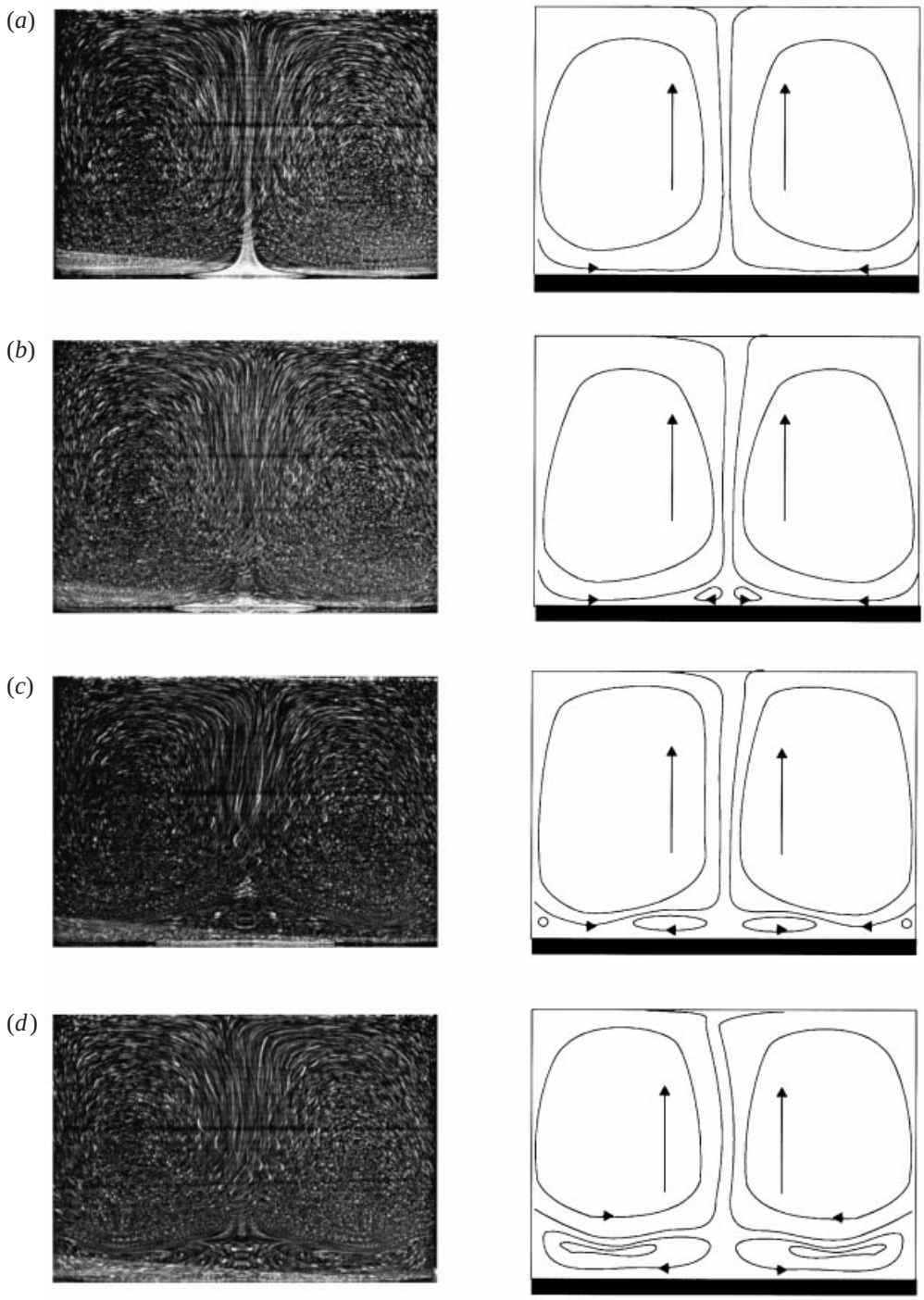

FIGURE 19. Streak photographs and pictorial representations of a xanthan gum Boger fluid for $H/R = 1.5$ showing (*a*) 'reverse' flow at $Re = 0.06$, $We = 8.17$, (*b*) central ring vortex at $Re = 0.12$, $We = 5.7$, (*c*) outside and central ring vortex at $Re = 0.36$, $We = 3.5$, and (*d*) combined ring vortex at $Re = 0.48$, $We = 3.0$.

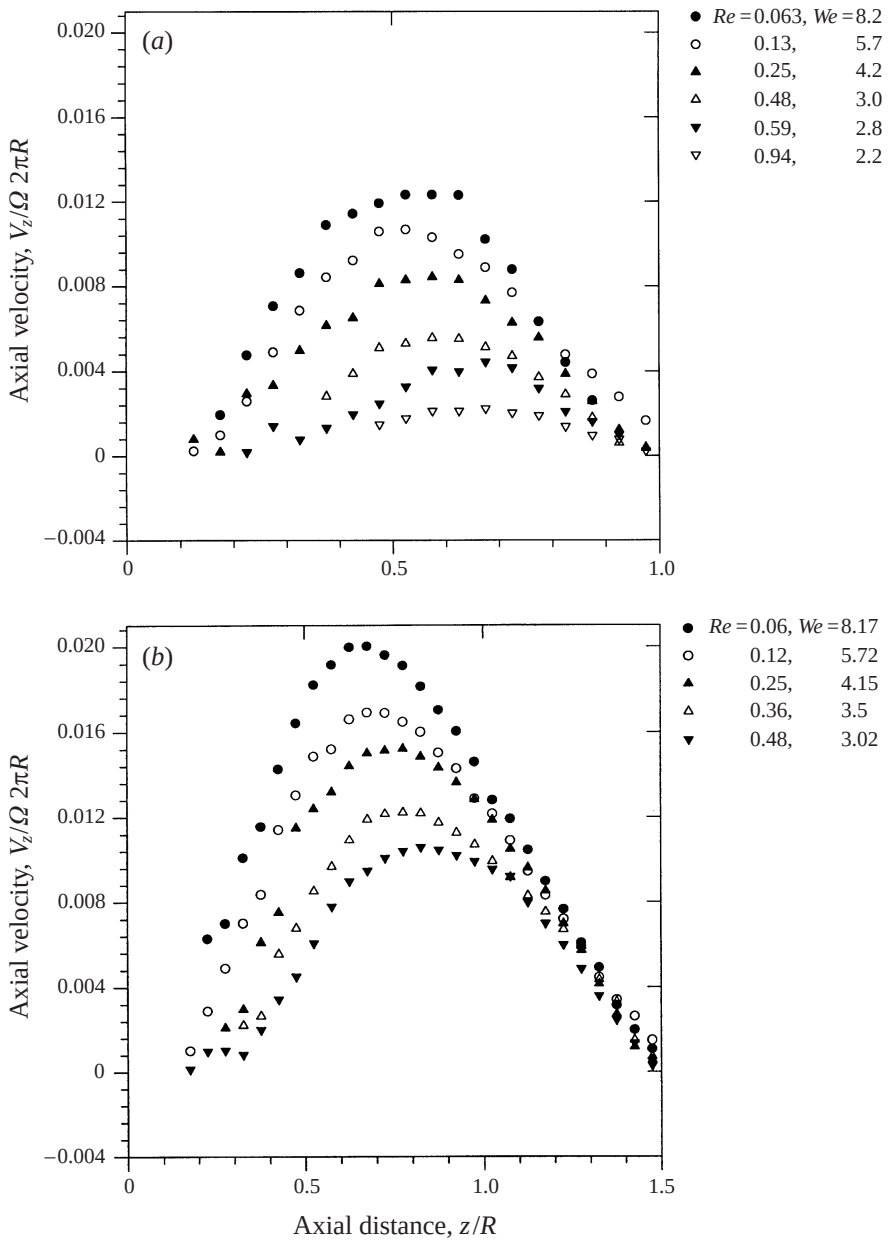

FIGURE 20. Dimensionless axial velocity along central axis ($r \approx 0$) for a xanthan gum Boger fluid at (*a*) $H/R = 1$, and (*b*) $H/R = 1.5$.

can only vary by a maximum factor of two and, hence, the viscosity was considered effectively constant. Therefore, shear thinning in the viscosity does not cause the outside ring vortex for the swirling flow of xanthan gum. However, it may be related to the variation in elasticity with shear rate owing to the non-constant relaxation time and also associated with orientation effects of the rigid macromolecules in the flow field.

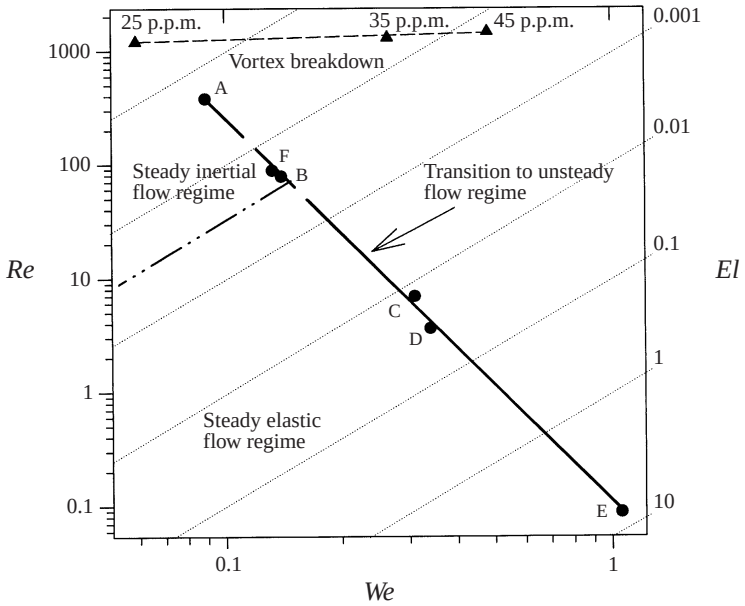

FIGURE 21. Stability boundary diagram for the confined swirling flow of polyacrylamide Boger fluids.

4. Discussion

The presence of small amounts of high molecular weight polymer (25–400 p.p.m.) in Newtonian solvents has been shown to influence the kinematics of confined swirling flow dramatically. The swirling flow of Boger fluids with elasticity numbers ranging across six orders of magnitude in Parts 1 and 2 using both a flexible and semi-rigid polymer has produced a wealth of flow phenomena owing to the competition between inertia, viscosity and elasticity. Elasticity, in the form of normal stress differences, in swirling flow attempts to drive the fluid in the opposite direction to the inertial centrifugal force that is generated by the rotating device. The normal stress difference acts as a tension along the curvilinear streamlines of the primary flow and subsequently causes a radial driving force which acts against centrifugal force. Hence, as the elasticity number is increased, the secondary flow transformed from 'Newtonian-like', where the flow is governed mainly by inertia, to a state which is flowing in the opposite direction and is driven by elasticity. A summary for the various flow phenomena observed for the polyacrylamide Boger fluids is given in table 5.

The following sections discuss the instabilities which are observed throughout the range of elastic polyacrylamide fluids, and compare the flow observed for flexible and semi-rigid polymer Boger fluids. Finally, the application of the results found in this work is discussed.

4.1. *Flow instability*

At least three types of flow instability have been observed in the swirling flow of polyacrylamide Boger fluids. The transitions to each of these instabilities are shown in figure 21 in terms of the Reynolds number and Weissenberg number, while the elasticity number is indicated by lines of 45°. The instabilities depend on the level of inertia and elasticity present in the flow field.

PAA fluid	*El*	*Re*	*We*	*H/R*
'Newtonian-like' flow				
A	0.0002	300	0.06	1, 1.5, 2
B	0.002	83	0.16	1, 1.5, 2
'Reverse' flow				
C	0.05	1.9	0.086	1, 1.5, 2
D	0.17	2	0.19	1, 1.8
E	10	0.044	0.4	1
Central ring vortex				
B	0.002	83	0.17	1, 1.5, 2
C	0.05	6.2	0.28	1, 1.5, 2
D	0.17	3.6	0.34	1, 1.8
E	10	0.088	0.88	1
Instability				
A	0.0002	378	0.089	1, 1.5, 2
B	0.002	83	0.17	1, 1.5, 2
C	0.05	6.9	0.31	1, 1.5, 2
D	0.17	3.6	0.61	1, 1.8
E	10	0.088	0.88	1

TABLE 5. Summary of secondary flow phenomena observed for polyacrylamide Boger fluids.

The inertial instability of vortex breakdown is examined in Part 1 with the existence domain of the low-viscosity polyacrylamide Boger fluids shown in figure 21 at an aspect ratio of $H/R = 1.5$. At low elasticity numbers and high Reynolds numbers, elasticity is shown to have a weak stabilizing effect on the steady inertial 'instability' mode of vortex breakdown. As the Weissenberg or elasticity number is increased by increasing the concentration of polyacrylamide, vortex breakdown is suppressed and does not occur for concentrations of 75 p.p.m. polyacrylamide.

The secondary-flow regime for all Boger fluids in Part 2 which contain dilute concentrations of flexible polyacrylamide is observed to become highly unstable once a critical combination of Reynolds number and Weissenberg number (or elasticity number) is reached for any particular fluid. The transition to unsteady behaviour is represented by a solid line in figure 21 where a clear correlation exists between the Reynolds number and Weissenberg number (or elasticity number). An additional data point from Stokes (1998) for a polyacrylamide Boger fluids (fluid F) is also included in the graph. Agreement to within $\pm 20\%$ of the stability line shown in figure 21 was found for all the medium- and high-viscosity polyacrylamide Boger fluids. This correlation for the occurrence of unsteady behaviour of the Boger fluids had a correlation coefficient of $r^2 = 0.995$ and is represented by the following relationship:

$$Re = 0.66\, El^{-0.\eta}. \tag{1}$$

This relation indicates that for polyacrylamide Boger fluids, the rotation rate required to cause as instability is a function of the fluid properties and flow geometry.

The elastic instabilities for the medium- and high-viscosity Boger fluids have been observed across a large range of flow states, and the relationship in equation (1) suggest that these effects are caused by similar mechanisms for the entire range of elasticity numbers. The flow kinematics of the various instabilities appear visually

different, but these differences may be attributed to the degree of inertia in the flow field. However, there is still clearly the presence of two elastic instability modes. The first is an inertio-elastic mode which occurs when inertia dominates the subcritical flow and the instability consists of intermittent flow reversal near the centre of the rotating disk. The flow reversal is seemingly aperiodic as elastic effects complete with inertial forces to cause an unsteady flow for polyacrylamide Boger fluids A, B and F. The second type of flow instability is a purely elastic mode which consists of a time-dependent spiral vortex which is wound by the primary flow up the centre of the cylinder. This instability is observed for Boger fluids C, D and E when the subcritical flow is dominated by elasticity.

The most common feature of all the elastic instabilities is a dramatic increase in the axial velocity along the central axis. This increase in axial velocity causes flow reversal for the cases where the subcritical flow is dominated by inertia, whereas when the subcritical flow is dominated by elasticity the magnitude of the axial velocity increases. The effects of the various degrees of inertia on the flow kinematics is further explored in Stokes (1998) where it is shown that the inertio-elastic mode observed for fluid F undergoes a transition to an elasticity dominated flow with an increase in rotation rate such that the elastic mode occurs. Stokes (1998) also shows that for an elastic shear-thinning fluid, the purely elastic instability mode transforms to the inertio-elastic mode as the Reynolds number is continually raised ($Re > 100$) and, hence, inertia increased.

The mechanism leading to instability of the swirling flow owing to the elasticity of the polyacrylamide fluids may be attributed to the non-Newtonian stress field and/or the interaction between the elastic and inertial stresses. The correlation in equation(1) extends down into the region where inertial effects are negligible ($Re \ll 1$) which infers that the purely elastic flow instabilities which are observed in other inertialess rotating flows are also due to these effects. Such flows include Taylor–Couette and co-axial disk flows where purely elastic flow instabilities are related to the radial driving force created by a large first normal stress difference acting along curvilinear streamlines (Larson 1992; Shaqfeh 1996; McKinley, Pakdel & Öztekin 1996). Joo & Shaqfeh (1992) also examine the influence of inertia on the viscoelastic instabilities in Taylor–Coutte flow. They observe an 'inertio-elastic' instability mode, using a linear stability analysis, which may be similar to that observed in this work. Further theoretical analysis of the instabilities observed in the confined swirling flow geometry is required to fully understand elastic instabilities which are observed in numerous situations involving swirl.

4.2. *Comparison between flexible and rigid polymers*

The differences between flow behaviour of rigid and flexible polymers are reflected in their different rheological properties. The shear-rate dependence of the primary normal stress difference for flexible polyacrylamide is quadratic at low shear rates and linear at high shear rates while semi-rigid xanthan gum has a square-root dependence. In extensional flow, polyacrylamide is extremely strain thickening while the extensional viscosity of xanthan gum is essentially constant with strain and strain rate. Therefore, polyacrylamide is more susceptible to the fluctuations in the rate of strain and stress gradients throughout the three-dimensional swirling flow field than xanthan gum. An instability is observed for polyacrylamide which has a substantial effect on the secondary-flow circulation such that the maximum axial velocity along the central axis increases markedly to be about 10% of the maximum azimuthal velocity. However, only a slight instability is observed for the xanthan gum Boger

fluid which did not have any noticeable effect on the axial velocity distribution. This instability occurs at Reynolds-number and elasticity-number combinations which are above the stability boundary in figure 21. An instability is also observed by Escudier & Cullen (1996) for semi-flexible carboxymethylcellulose at conditions which closely match the boundary line in figure 21. However, this instability is not as dominant on the secondary flow as that for polyacrylamide. The instantaneous state of stress is a function of the history of deformation and the magnitude of deformation for viscoelastic fluids (Larson 1992). Hence, the strong dependence of the viscoelastic material functions on the rate-of-strain for polyacrylamide compared to xanthan gum, will mean it is more susceptible to temporal variations in local fluid stress or straining motions and, therefore, more likely to become unstable.

4.3. *Applications*

The investigation into confined swirling flow of non-Newtonian fluids is highly relevant to process industries where swirling flows are used. Figure 21 shows that it is possible to obtain a highly unsteady flow for very viscous and elastic fluids at very low Reynolds numbers ($Re < 1$) which is favourable in any mixing process involving swirl. It would be expected that any fluid with rheological properties comparable to polyacrylamide will behave in a similar manner and, hence, the confined swirling apparatus may be a useful mixing device.

The numerical prediction of the flow behaviour of elastic fluids in complex mixing geometries is ultimately desirable for many engineering applications. However, numerical codes and constitutive equations must be established and validated with well-characterized experimental information, now presented in this paper. Constant-viscosity elastic fluids were used to separate effects associated with elasticity from shear thinning, and situations were investigated where inertia is both dominant and negligible to enable prediction across a broad spectrum of circumstances. Several observations include instabilities of a time-periodic and three-dimensional nature which would be difficult to predict accurately in a numerical model. However, it will now be easier to control and understand the influence of elasticity on the axis-symmetric vortex breakdown in inertia-dominated flows. The prediction of steady 'reverse' flow, counter-rotating ring vortices on the rotating lid, and the influence of elasticity on axis-symmetric vortex breakdown should provide highly beneficial data for numerical prediction before solving the unsteady flows of viscoelastic fluids.

5. Conclusion

In the confined swirling flow of constant-viscosity elastic fluids dilute concentrations of flexible polyacrylamide or semi-rigid xanthan gum, the secondary-flow regime is dramatically altered owing to the influence of fluid elasticity. Normal stresses acting as a tension along the curvilinear primary-flow streamlines cause an elastic force to act against the inertial force. As the level of elasticity is increased by using a series of flexible polymer solutions, the flow transforms from being the 'Newtonian-like', where the secondary motion is directed radially outwards along the rotating lid, to being elasticity driven, where the secondary motion is in the opposite direction to that for Newtonian fluids. Several complex secondary-flow patterns are observed which depend on the level of elasticity and inertia, the polymer type and conformation, and the cylinder aspect ratio. In Part 1, the well-known inertial vortex breakdown instability is shown to be stabilized through weak elastic effects, whereas in Part 2 elasticity is shown to cause a new elastic time-dependent instability which is slightly

destabilized by inertial effects. A correlation between the critical Reynolds number and elasticity number (or Weissenberg number) for the elastic instability has been found for the polyacrylamide Boger fluids which is valid in circumstances when inertia is either dominant or negligible. Material parameters in single mode and multi-mode Oldroyd-B, FENE-P, Giesekus and KBKZ constitutive models have been used to describe the rheology for the polyacrylamide Boger fluids. The results from the flow-visualization experiments of the rheologically well-characterized Boger fluids will enable the validation of numerical predictions in the confined swirling flow as a test case of non-Newtonian constitutive models.

The authors would like to thank Brook Dunstan from CSIRO BCE for his assistance in obtaining good quality photographs, Dr Duc At Nguyen and Professor Tam Srihdar from Monash University for measurements of the extensional viscosity using the filament-stretching device, and Andrew Brydon from Monash University for providing the results from his numerical model of the Navier–Stokes equations in the torsionally driven cavity. The work on viscoelastic fluid mechanics at the University of Melbourne is supported by a Special Investigation Grant of the Australian Research Council.

REFERENCES

Bernstien, B., Kearsley, E. A. & Zapas, L. 1963 A study of stress relaxation with finite strain. *Trans. Soc. Rheol.* **7**, 391–410.

Bird, R. B., Armstrong, R. C. & Hassanger, O. 1987*a* *Dynamics of Polymeric Liquids. Volume 1: Fluid Mechanics*, 2nd edn. Wiley Interscience.

Bird, R. B., Curtiss, C. F., Armstrong, R. C. & Hassanger, O. 1987*b* *Dynamics of Polymeric Liquids. Volume 2: Kinetic Theory*, 2nd edn. Wiley Interscience.

Bird, R. B., Dotson, P. J. & Johnson, N. L. 1980 Polymer solution rheology based on a finitely extensible bead-spring chain model. *J. Non-Newtonian Fluid Mech.* **7**, 213–235.

Bird, R. B. & Weist, J. M. 1985 Anisotropic effects in dumbbell kinetic theory. *J. Rheol.* **29**, 519–532.

Boger, D. V. 1977/78 A highly elastic constant viscosity fluid. *J. Non-Newtonian Fluid Mech.* **3**, 87–91.

Böhme, G., Rubart, L. & Stenger, M. 1992 Vortex breakdown in shear-thinning liquids: experiment and numerical simulation. *J. Non-Newtonian Fluid Mech.* **45**, 1–20.

Brydon, A. & Thompson, M. 1998 A trapped wave model for confined vortex breakdown. In *Proc. 13th Australasian Fluid Mech. Conf.* In press.

Byars, J. A., Binnington, R. J. & Boger, D. V. 1997 Entry flow and constitutive modelling of fluids S1. *J. Non-Newtonian Fluid Mech.* **72**, 219–235.

Chiao, S. M. F. & Chang, H. C. 1990 Instability of a Criminale–Ericksen–Filbey fluid in a disk-and-cylinder system. *J. Non-Newtonian Fluid Mech.* **36**, 361–394.

Day, C., Harris, J. A., Soria, J., Boger, D. V. & Welsh, M. C. 1996 Behaviour of an elastic fluid in cylindrical swirling flow. *Expl Therm. Fluid Sci.* **12**, 250–255.

Escudier, M. P. & Cullen, L. M. 1996 Flow of a shear-thinning liquid in a cylindrical container with a rotating end wall. *Expl Therm. Fluid Sci.* **12**, 381–387.

Giesekus, H. 1982 A simple constitutive equation for polymeric fluids based on the concept of configuration-dependent tensorial mobility. *J. Non-Newtonian Fluid Mech.* **11**, 69–109.

Giesekus, H. 1983 Stressing behavior in simple shear flow as predicted by a new constitutive model for polymer fluids. *J. Non-Newtonian Fluid Mech.* **12**, 367–374.

Hill, C. T. 1972 Nearly viscometric flow of viscoelastic fluids in the disk and cylinder system. II: Experimental. *Trans. Soc. Rheol.* **16**, 213–245.

Joo, Y. L. & Shaqfeh, E. S. G. 1992 The effects of inertia on the viscoelastic Dean and Taylor–Couette flow instabilities with application to coating flows. *Phys. Fluids* A **4**, 2415–2431.

KAYE, A. 1962 Non-Newtonian flow in incompressible fluids. Note no. 134, College of Aeronautics, Cranfield.

KRAMER, J. M. & JOHNSON, M. W. 1972 Nearly viscometric flow in the disk and cylinder system. I: Theoretical. *Trans. Soc. Rheol.* **16**, 197–212.

LARSON, R. G. 1992 Instabilities in viscoelastic flows. *Rheol. Acta* **31**, 213–263.

MCKINLEY, G. H., PADKEL, P. & ÖZTEKIN, A. 1996 Rheological and geometric scaling of purely elastic flow instabilities. *J. Non-Newtonian Fluid Mech.* **67**, 19–47.

NIRSCHL, J. P. & STEWART, W. E. 1984 Computation of viscoelastic flow in a cylindrical tabk with a rotating lid. *J. Non-Newtonian Fluid Mech.* **16**, 233–250.

OLDROYD, J. G. 1950 On the formation of rheological equations of state. *Proc. R. Soc.* A **200**, 523–541.

ORR, N. V. & SRIHDAR, T. 1996 Stress relaxation in uniaxial extension. *J. Non-Newtonian Fluid Mech.* **67**, 77–103.

PAPANASTASIOU, A. C., SCRIVEN, L. E. & MACOSKO, C. W. 1983 An integral constitutive equation for mixed flows: viscoelastic characterization. *J. Rheol.* **27**, 387–410.

PETERLIN, A. 1966 Hydrodynamics of linear macromolecules. *Pure Appl. Chem.* **12**, 563–586.

SHAQFEH, E. S. G. 1996 Fully elastic instabilities in viscometric flow, *Ann. Rev. Fluid Mech.* **28**, 129–185.

SIGNER, A. 1991 Viscoelastic swirling flow with free surface in cylindrical chambers. *Rheol. Acta* **30**, 159–174.

SPEILGELBEREG, S. H. & MCKINLEY, G. H. 1996 Stress relaxation and elastic decohesion of viscoelastic polymer solutions in extensional flow. *J. Non-Newtonian Fluid Mech.* **67**, 49–76.

STOKES, J. R. 1998 Swirling flow of viscoelastic fluids. PhD dissertation, University of Melbourne.

STOKES, J. R., DUNSTUN, B., GRAHAM, L. J. W. & BOGER, D. V. 1995 Observations of an elastic liquid in confined swirling flow. *Album of Visualisation* **21**, 5–6.

STOKES, J. R., GRAHAM, I. J. W., LAWSON, N. J. & BOGER, D. V. 2001 Swirling flow of viscoelastic fluids. Part 1. Interaction between inertia and elasticity. *J. Fluid Mech.* **429**, 67–115.

TIRTAATMADJA, V. 1993 Measurement of extensional viscosity of polymer solutions. PhD dissertation, Monash University.

TIRTAATMADJA, V. & SRIDHAR, T. 1993 A filament stretching device for measurement of extensional viscosity. *J. Rheol.* **37**, 1081–1102.

TIRTAATMADJA, V. & SRIDHAR, T. 1995 Comparison of constitutive equations for polymer solutions in uniaxial extension. *J. Rheol.* **39**, 1133–1160.

WARNER, H. R. 1972 Kinetic theory and rheology of dilute suspension of finitely extensible dumbbells. *Ind. Engng Chem. Res.* **27**, 379–387.

WÜSCH, O. & BÖHME, G. 1996 On torsionally driven viscoelastic flow in a cylindrical vessal. In *Proc. XIIth Intl Congr. on Rheology* (ed. A. Ait-Kadi, J. M. Dealy, D. F. James & M. C. Williams), pp. 846–848. Laval University.